STUDIA

UNIVERSITATIS
BABEŞ-BOLYAI

Physica

CLUJ-NAPOCA 2006

2

Cluj University Press

EDITORIAL BOARD OF

STUDIA UNIVERSITATIS BABEŞ-BOLYAI PHYSICA

EDITORIAL OFFICE OF PHYSICA: M. Kogălniceanu no. 1, 400084 Cluj-Napoca, Phone 0264-405300

ANUL LI **2006**

S T U D I A
UNIVERSITATIS BABEŞ–BOLYAI
PHYSICA
2

Editorial Office: 400015 – Cluj–Napoca Republicii no. 24, Phone: 0264-405352

SUMAR - SOMMAIRE - CONTENTS - INHALT

STUDIA UNIVERSITATIS BABEŞ-BOLYAI, PHYSICA, LI, 2, 2006

FT-IR AND RAMAN SPECTROSCOPIC STUDY OF Li_2O-CuO-TeO_2 GLASSES

CARMEN MARCUS[*], R. CICEO LUCACEL AND I. ARDELEAN

ABSTRACT. The local structure of the $xLi_2O\cdot(1-x)[2TeO_2\cdot CuO]$ ($0 \le x \le 0.5$) glass system was investigated by means of FT-IR and Raman spectroscopies. For the glass network was proposed a structure mainly composed of TeO_4 trigonal bipyramids (tbp), TeO_3 trigonal pyramids (tp) and TeO_{3+1} polyhedral units. It was found that with the increase of Li_2O content the modification of tellurite network consist in the conversion of a part of TeO_4 tbp into TeO_3 tp via intermediate coordination TeO_{3+1} polyhedra. Simultaneously the nonbridging oxygens (NBOs) number increases, denoting the depolymerization of the glass structure.

Keywords: Lithium-copper-tellurite glasses, FT-IR, Raman

Introduction

Tellurium oxide under normal condition does not have the ability to form glasses easily without a modifier like an alkali oxide, an alkaline-earth oxide, a transition-metal oxide or a glass former [1]. Tellurite based glasses are of scientifically and technologically interest because of their low melting temperature, high dielectric constant, high refractive indices, high thermal-expansion coefficient, thermochromic properties [2 - 4] and good transmission for infrared (IR) lights with a wide range of wavelength [5]. All these properties determine different applications for tellurite glasses: in solid state batteries, fuel cells, optical fibres, gas sensors, infrared filters and host materials for laser applications [6, 7]. Their nonlinear susceptibility is the highest among the known glasses. The microscopic origin of this property is still far from final clarity, but there is no doubt that it would directly relate to the peculiarities of the valence electron distribution and short-range structural arrangement [8].

The structure of TeO_2-based glasses has been frequently studied by means of Raman scattering [3, 4, 9 - 14] and IR spectroscopy [3, 10, 11, 15, 16], reporting that is built up from three types of structural units such as TeO_4 tbp, with two equatorial and two axial Te-O bonds, TeO_{3+1} polyhedra and TeO_3 tp [2, 3, 5, 17]. The concentration of the characteristically structural units and the transformation of TeO_4 tbp to TeO_{3+1} and TeO_3 tp units is strongly affected by the glass composition, the type and concentration of network modifier as

---

[*] Faculty of Physics, Babes-Bolyai University, 400084, Cluj-Napoca, Romania
Corresponding author’s E-mail: cmarcus@phys.ubbcluj.ro

well by other causes [1, 9, 18]. The addition of transition-metal oxide (CuO for example) to tellurite glasses gives them specific semiconducting and magnetic properties [1, 19]. Lithium oxide addition in the tellurite glasses determines an increase in their ionic conductivity [7].

The aim of present study was to obtain information concerning the local structure of lithium doped $2TeO_2$-CuO glasses by means of FT-IR absorption and Raman scattering.

Experimental details

To prepare the glass samples from the $xLi_2O\cdot(1-x)[2TeO_2\cdot CuO]$ ($0 \leq x \leq 0.5$) system the conventional melt quenching technique was used. All glass samples were prepared in similar conditions from reagent grade purity Li_2CO_3, TeO_2 and CuO in suitable proportion. The mechanically homogenized mixtures were melted in sintered corundum crucibles placed in an electrical furnace at 1000°C for 6 minutes. The mixtures were introduced directly in the preheated furnace at this temperature to avoid losses due to the evaporation. The homogenized melt was then cast quenched between two stainless-steel plates.

The FT-IR absorption spectra were recorded with an Equinox 55 Bruker spectrometer, using the KBr pellet technique. In order to obtain good quality spectra the samples were crushed in an agate mortar to obtain particles of micrometer size. This procedure was applied every time to fragments of bulk glass to avoid structural modifications due to ambient moisture. The spectral resolution used for the recording of the FT-IR spectra is 2 cm^{-1}.

Raman spectra of the samples were recorded with a Dilor Raman spectrometer (Horiba-Jobin-Yvon, model LabRam) using the 514.5 nm radiation from a Spectra Physics argon ion laser for excitation. The Raman signal was detected with a charge coupled device (CCD) camera (Photometric Model 9000). Raman spectra were recorded using a laser power of 100 mW, in the back-scattering geometry with a resolution of 2 cm^{-1}.

All measurements were performed at room temperature.

Results and discussion

Figure 1 shows the FT-IR spectra of $xLi_2O\cdot(1-x)[2TeO_2\cdot CuO]$ glasses where x takes values from 0 to 0.5, in the spectral range 400 - 900 cm^{-1}. The bands obtained in the FT-IR absorption spectra and their assignments are summarized in Table I. The assignments were made comparing the experimental data of the studied glasses with those of related crystalline and vitreous compounds [7, 10, 14, 18, 20 - 22].

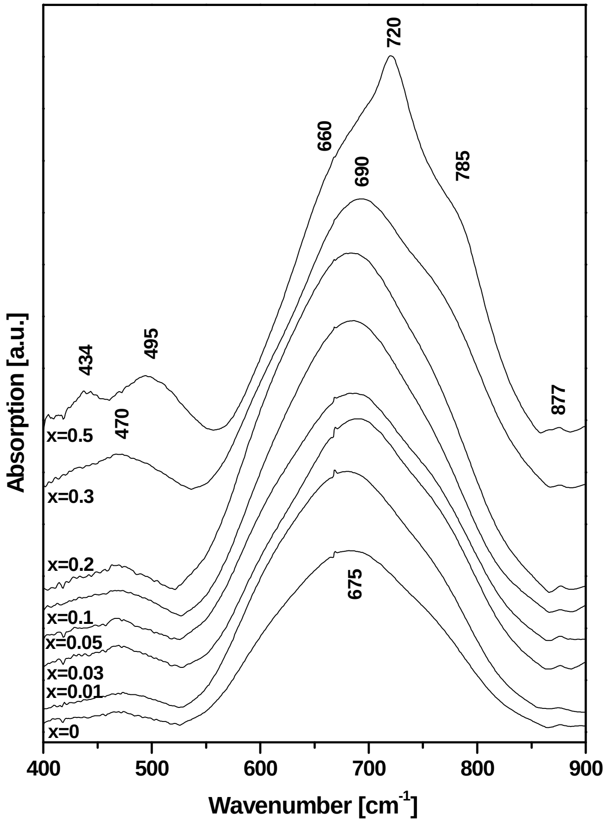

Fig. 1. FT-IR spectra of $xLi_2O\cdot(1-x)[2TeO_2\cdot CuO]$ glasses

The FT-IR spectrum of the $2TeO_2$-CuO glass matrix reveals a weak band positioned at 470 cm^{-1}, a strong band placed at 675 cm^{-1} and a weak band sited at 877 cm^{-1}. From the assignments of the detected FT-IR absorption bands (Table I) was concluded that in the structure of the glass matrix the predominant units are TeO_4 tbp evidenced by the strong band at 675 cm^{-1}. The presence of TeO_3 tp is revealed by the weak band positioned at 877 cm^{-1}.

With the Li_2O addition to the $2TeO_2$-CuO glass matrix the FT-IR spectra show some changes regarding the network structure. When the Li_2O content reaches the value 0.5, in the spectrum of this sample was detected a new absorption band position at 434 cm^{-1}, assigned to the vibrations of Te-O-Te bridging bond in TeO_4 tbp units. This band was not observed for the previous Li_2O concentrations. The band positioned at 470 cm^{-1} is present in the FT-IR spectra of the glass samples where x take values from 0 to 0.3.

Table I.
Assignments of the FT-IR and Raman bands in the spectra of $xLi_2O\cdot(1-x)[2TeO_2\cdot CuO]$ glasses

Peak positions (cm^{-1})		**Assignment**	
FT-IR	*Raman*	*FT-IR*	*Raman*
~ 434	~ 330	Vibrations of Te-O-Te bridging bond in TeO_4 tbp units	Bending vibrations of TeO_3 tp units with NBOs
~ 470 ~ 495	~ 384	Symmetric Te-O-Te linkage vibrations	Symmetric vibrations of the simple Te-O-Te bridges
~ 660	~ 455	Vibrations of T-O in TeO_{3+1} units	Bending vibrations of Te-O-Te or O-Te-O linkages in TeO_4 tbp units
~ 675	~ 632	Symmetrical stretching vibrations of Te-O-Te in TeO_4 tbp units with bridging oxygen	Stretching vibrations of Te-O-Te linkages from TeO_4 tbp and TeO_{3+1} polyhedra
~ 720	~ 714 ~ 743	Stretching vibrations of TeO_3 tp or TeO_{3+1} polyhedra with NBOs	Stretching vibrations mode of TeO_3 tp with NBOs
~ 785 ~ 877	~ 754 ~ 778	Stretching vibration mode of TeO_3 tp with NBOs	Stretching vibrations of Te-O of TeO_3 tp and a small amount of TeO_4 tbp with NBOs

With the increases of Li_2O content from 0.3 to 0.5 was observed a shift of the 470 cm^{-1} absorption band to a higher wavenumber 495 cm^{-1} denoting that the distortion of the TeO_4 units become larger. The weak shoulder at 660 cm^{-1} is more obvious with lithium oxide addition, suggesting that the amount of TeO_{3+1} polyhedra units increases. The band at 675 cm^{-1} assigned to the symmetrical stretching vibrations of Te-O-Te in TeO_4 tbp units with bridging oxygen dominates the spectra in the 0 - 0.2 compositional range. This band is shifted towards higher wavenumber 690 cm^{-1} ($x = 0.3$) due to an enhancement of the polymerization degree of the TeO_2 network or to an increase in the formation of the TeO_{3+1} structural units. The band at 690 cm^{-1} is overlap by the new strong band at 720 cm^{-1}, detected only for the sample with $x = 0.5$. Furthermore, the elongation of Te-O bond of TeO_{3+1} and its cleavage finally leads to the formations of TeO_3 tp units. The existence in the sample ($x = 0.5$) spectrum of the 720 cm^{-1} band is the prove that changes in the coordination of tellurium atoms from 4 to 3 take place through the so-called 3+1 intermediate environment, along with the increases number of nonbridging oxygens (NBOs) [7, 11, 12, 23]. The presence of the shoulder at 785 cm^{-1} and the weak quantity

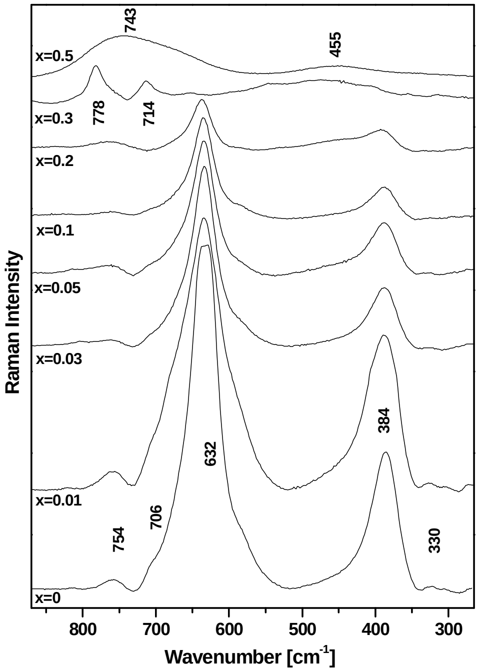

Fig. 2. Raman spectra of $xLi_2O\cdot(1-x)[2TeO_2\cdot CuO]$ glasses

implies an increase in intensity of the detected absorption bands denoting the increases number of the NBOs in the glass network, concomitantly with a continuous and progressive deformation of the Te environment (by shortening of one of the two axial bonds and, conversely, a lengthening of the other). In all the compositional range 0 - 0.5 in the glass structure the amount of the units were tellurium is 4 coordinated is higher than the one in which is 3 coordinated.

The recorded experimental Raman spectra of the $xLi_2O\cdot(1-x)[2TeO_2\cdot CuO]$ glass system, with various content of Li_2O ($0 \leq x \leq 0.5$) are shown in figure 2. Table I presents the assignments of the bands detected in the Raman spectra.

In the Raman spectrum of the $2TeO_2$-CuO glass matrix, were observed: a weak band placed at 330 cm^{-1}, a medium band positioned at 384 cm^{-1}, a strong band at 632 cm^{-1}, a shoulder at 706 cm^{-1} and also a weak band at 754 cm^{-1}. The existence of the three structural units detected through Raman scattering namely TeO_4 tbp (evidenced by the presence of the band at 632 cm^{-1}), TeO_3 tp (confirmed by the bands at 330 cm^{-1} and 754 cm^{-1}), and TeO_{3+1} polyhedra (supported by the band at 632 cm^{-1}) is in agreement with the results gave by the FT-IR data.

Controlled addition of Li_2O determines a decrease in the amount of the TeO_4 tbp units evidenced by the decrease intensity of the bands centered at 632 cm^{-1}. Both TeO_4 tbp and TeO_3 tp units containing terminal Te-O bonds such as Te=O and $Te\text{-}O^-$ with NBOs [9, 24] ($x \le 0.2$) are evidenced by the existence of the band at 754 cm^{-1}. The decrease intensity of this band is due to the spatial rearrangement of TeO_4 tbp units with low symmetry. The progressively Li_2O additions implies a decrease in the Raman bands intensity indicating the increases of vitreous network depolymerization degree and a continuously change of the glass structure from TeO_4 tbp to TeO_3 tp units via intermediate species TeO_{3+1}. Simultaneous, the number of nonbridging oxygens (NBOs) increases. In the 0 - 0.2 compositional range the predominant units in the samples structure are the TeO_4 trigonal bypiramidal.

The new weak band at 455 cm^{-1} ($x = 0.3$) is most often assigned to the bending vibrations of Te-O-Te or O-Te-O linkages which are formed by vertex sharing of TeO_4 tbp basic structural units [5]. For $x = 0.3$ the bands at 330, 384 and 632 cm^{-1} disappear from the spectrum, while the shoulder at 706 cm^{-1} and the band at 754 cm^{-1} are shifted to a higher wavenumber 714 cm^{-1} and 778 cm^{-1}, respectively. In the sample structure the quantity of TeO_3 trigonal pyramids units increase in disfavor of the TeO_4 trigonal bipyramids one, according with the assignment made for the detected Raman bands.

For higher Li_2O content ($x = 0.5$) the Raman spectrum consist only in a weak band (455 cm^{-1}) and a broad envelop of the 714 cm^{-1} and 778 cm^{-1} bands (centered at 743 cm^{-1}). The TeO_4 tbp units are still present in the sample structure but in a small amount, while the TeO_3 tp units become the predominant units in the lattice. The TeO_3 has a lone pair of electrons. In the TeO_3 tp, therefore, the spatial occupation probability of this lone pair of electrons increase compared with the TeO_4 tp. Increasing amount of TeO_3 tp groups causes the repulsion between TeO_3 and TeO_4 groups or within TeO_3 groups in additions to a decrease in number of bridging bonds [23]. The TeO_3 tp restrict the spatial arrangements of structural units and deteriorate glass formation [23, 25]. No characteristic bands for Li-O or Cu-O link vibrations were found.

Conclusion

FT-IR and Raman measurements were performed in order to elucidate the local structure of $xLi_2O\cdot(1-x)[2TeO_2\cdot CuO]$ ($0 \le x \le 0.5$) glasses and the changes that occur with Li_2O addition. The Li_2O-$2TeO_2$-CuO glass system present characteristic tellurium atoms and their coordination changes with the increases of Li_2O content from TeO_4 trigonal bipyramids to TeO_3 trigonal pyramids and TeO_{3+1} polyhedra, simultaneously with the increases number of nonbridging oxygens (NBOs). Also, the structure is depolymerized. In the glass matrix the amount of TeO_4 units is superior to that of TeO_3 units. The Li_2O addition implies a rearrangement in the glass structure through the transformation of some TeO_4 tbp to TeO_{3+1} and TeO_3 tp structural units. This conversion is made by shortening of one of the axial bond while one equatorial bond gets longer (TeO_{3+1} polyhedra) when the modifier content increases. The Li_2O oxide acts as a glass modifier in the studied glasses, information confirmed by both FT-IR and Raman techniques.

REFERENCES

1. M. A. Salim, G. D. Khattak, N. Tabet, L. E. Wenger, *J. of Elect. Spec.*, **128** (2003) 75.
2. S. Suehara, S. Hishita, S. Inoue, A. Nukai, *Phys. Rev. B*, **58**(21) (1998) 14 124.
3. L. C. Sabadel, P. Armand, D. Cachau-Herreillat, P. Baldeck, O. Doclot, A. Ibanez, E. Philippot, *J. Solid State Chem*., **132** (1997) 411.
4. H. Li, Y. Su, S. K. Sundaram, *J. Non-Cryst. Solids*, **293-295** (2001) 402.
5. Y. Iwadate, M. Suzuki, T. Hattori, K. Fukushima, S. Nishiyama, M. Misawa, T. Fukunaga, K. Itoh, *J. Alloys and Compounds*, **389** (2005) 229.
6. C. Duverger, M. Bouzaoui, S. Turrell, *J. Non-Cryst. Solids*, **220** (1997) 169.
7. K. Muruganandam, M. Seshasayee, *J. Non-Cryst. Solids*, **222** (1997) 131.
8. A. P. Mirgorodsky, T. Merle-Mejean, J. - C. Champarnaud, P. Thomas, B. Frit, *J. Phys. Chem. Solids*, **61** (2000) 501.
9. R. Ciceo Lucacel, I. Ardelean, *Phys. Chem. Glasses*, **45(4)** (2004) 295.
10. B. V. R. Chowardi, K. L. Tan, Fang Ling, *J. Mat. Sciences*, **35** (2000) 2015.
11. L. Baia, M. Bolboaca, W. Kiefer, E. S. Yousef, C. Rüssel, F. W. Breitbarth, T. G. Mayerhöfer, J. Popp, *Phys. Chem. Glasses*, **45**(3) (2004) 178.
12. T. Sekiya, N. Mochida, S. Ogawa, *J. Non-Cryst. Solids*, **185** (1995) 135.
13. P. Charton, P. Armand, *J. Non-Cryst. Solids*, **333** (2004) 307.
14. Q. J. Rong, A. Osaka, T. Nanba, J. Takada, Y. Miura, *J. Mat. Science*, **27** (1992) 3793.
15. P. Charton, P. Thomas, P. Armand, *J. Non-Cryst. Solids,* **321** (2003) 81.
16. A. Abd El-Moneim, *Mat. Chem. Phys*., **73,** (2002) 318.
17. C. Y. Wang, Z. X. Shen, B. V. R. Chowdari, *J. Raman Spectrosc*., **29** (1998) 819.
18. R. F. Cuevas, L. C. Barbosa, A. M. de Paula, Y. Liu, V. C. S. Reynoso, O. L. Alves, N. Aranha, C. L. Cesar, *J. Non-Cryst. Solids*, **191** (1995) 107.
19. G. D. Khattak, A. Mekki, L. E. Wegner, *J. Non-Cryst. Solids*, **337** (2004) 174.
20. T. Sekiya, N. Mochida, A. Ohtsuka, A. Soelimi, *J. Non-Cryst. Solids*, **151** (1992) 222.
21. I. Shaltout, Y. Tang, R. Braunstein, A. M. Abu-Elazm, *J. Phys. Chem. Solids*, **56** (1995) 141.
22. J. C. Champarnaud-Mesjard, S. Blanchandin, P. Thomas, A. Mirgorodsky, T. Merle-Mejean, B. Frit, *J. Phys. Chem. of Solids*, **61** (2000) 1499.
23. J. Zhang, J. Qui, Y. Kawamoto, *Mat. Letters*, **55** (2002) 77.
24. S. Khatira, J. Bolka, B. Capoen, S. Turrell, M. Bouazaoui, *J. Molecular Structure,* **563-564** (2001) 283.
25. Y. Himei, Y. Miura, T. Nanba, A. Osaka, *J. Non-Cryst. Solids*, **211** (1997) 64.

STUDIA UNIVERSITATIS BABEŞ-BOLYAI, PHYSICA, LI, 2, 2006

LOCAL STRUCTURE OF $3B_2O_3$-PbO-Ag_2O BASED GLASSES ANALYZED THROUGH RAMAN SPECTROSCOPY

A. O. HULPUS*, R. CICEO LUCACEL AND I. ARDELEAN

ABSTRACT. Glasses from $xCuO\cdot(1-x)[3B_2O_3\cdot(1-y)PbO\cdot yAg_2O]$ ($0 \le x \le 0.1$ and $y = 0.1, 0.3$) system were prepared and studied by means of Raman scattering. For both systems were found bands characteristic to borate based glasses structure such as: boroxol rings, diborate, pyroborate and metaborate groups. It was evaluated the influence of both Ag_2O/PbO ratio and CuO variation on the short-range order (SRO) of the network in order to obtain information concerning the local structure of copper-doped $3B_2O_3$-PbO-Ag_2O glass matrices. Increasing the Ag_2O/PbO ratio induces a higher degree of glass network disorder. Controlled addition of cooper ions determined a decrease in the intensity of the borate Raman bands for both systems denoting a progressively disorder of their vitreous network.

Keywords: Cooper-silver-lead-borate glasses, Raman

Introduction

Borate glasses have unexpected properties, which cannot easily be predicted and in many cases are difficult to interpret. This behavior is due to the presence of the boron anomaly: the boron atom can be found in the network, in trigonal or tetrahedral coordination depending on the concentration of the modifier oxide [1-3]. Due to their high refractive indices, high resistance ag44ainst devitrification and low melting temperature, glasses containing lead oxide have many applications as optical lenses, electronic devices and simulated Raman fiber amplifiers [4]. According to previous results, lead oxide enters into the network in three and /or four-coordinated positions. Depending on the concentrations, it acts either as modifier or as network former [3, 5-7]. Glasses containing Ag^+ ions have important technological properties presenting high ionic conductivity with the prospect of producing glasses that are superionic conductors. On the other hand, glasses with small quantities of silver oxide have the desired characteristics for photochromic lenses, solid electrolytes and chemical sensors [8-11]. The addition of copper oxide to the B_2O_3-PbO-Ag_2O ternary glass system is motivated by the fact that CuO gives great fluidity without increasing thermal expansion. In addition, the coexistence of copper in two different oxidation states in the glasses is important for technical applications, for soldering and integrated circuit (IC) packaging [12]. The local structure of the B_2O_3-PbO glass system was the subject of many FT-

---

* Faculty of Physics, Babes Bolyai University, Cluj Napoca, 40008, Romania
Corresponding author's: E-mail: ahulpus@phys.ubbcluj.ro

IR, 44Raman Mössbauer studies, density and electrical measurements [3, 5-7, 13-15]. Up to 50 mol % PbO content it acts as a network modifier leading to the formation of BO_4 units which along with the presence of BO_3 units are placed in borate arrangements such as: diborate groups, triborate, tetraborate, and pentaborate groups. On the other hand above 50 mol % PbO there is an increase of the non bridging oxygen's (NBOs); the latter consists in chain- and ring-type metaborate at the expense of BO_4 units [16].

The aim of the present work is to evaluate the influence of both Ag_2O/PbO ratio and x variation on the local $xCuO\cdot(1-x)[3B_2O_3\cdot(1-y)PbO\cdot yAg_2O]$ glasses structure.

Experimental procedure

The prepared glass compositions were $xCuO\cdot(1-x)[3B_2O_3\cdot(1-y)PbO\cdot yAg_2O]$ with $0 \leq x \leq 0.1$ and $y = 0.1$ and 0.3. The batch of the mixture of the reagent grade H_3BO_3, PbO, $AgNO_3$ and CuO was melted in air, in sintered corundum crucibles, in an electric furnace at 950°C for 15 minutes. The melts were quickly cooled at room temperature by pouring them onto stainless steel plates. The Raman spectra were recorded for bulk glasses using a LabRam spectrometer in back-scattering (90°) geometry with a resolution of 4 cm^{-1} at room temperature using for excitation the 514.5 nm of a Spectra Physics argon ion laser with an output power of 50 mW.

Results and discussion

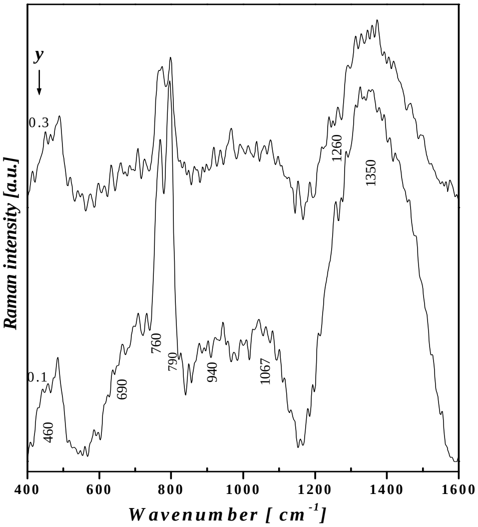

Fig 1. Raman spectra of $3B_2O_3\cdot(1-y)PbO\cdot yAg_2O$ glasses

Raman measurements made on the vitreous B_2O_3 shown that the glass network structure is based on boroxol rings interconnected by a small proportion of BO_3 units [4]. The changes that occur in the glass structure with the addition of lead and silver oxide are exposing by the presence of new bands coming from the modified borate network.

The Raman spectrum of the matrix with y = 0.1 (Fig. 1) is dominated by a broad band (1350 cm^{-1}), three well defined bands (460, 760 and 790 cm^{-1}) and four other signals (690, 940 1067 and 1260 cm^{-1}). The assignments of the Raman ba4n4ds, listed in table I, expose a glass network mainly based on BO_3 units disposed in boroxol rings, metaborate groups, $BØ_2O^-$ triangles linked to $BØ_4^-$ units, isolated or placed in six membered ring types, diborate and pyroborate groups.

The band corresponding to symmetric breathing vibration of the boroxol rings which generally appears at 806 cm^{-1} is shifted to a lower wavenumber (790 cm^{-1}); the change in the wavenumber depends on the kind and concentration of the network modifiers. This assumption is based on the results obtained by our research group on several glass systems that contain silver oxide and lead oxide (since in B_2O_3-PbO glasses this tendency was not evidenced) [13, 14, and 17]. The shift to a lower wavenumber caused by a distortion of the boroxol rings is probably due to a decrease of the bond force constant. The fact that the Raman spectrum show well defined bands implies the existence of a relatively high degree of ordering inside the short range limits in the glass network.

Table 1.

Assignments of the Raman bands in the spectra of $xCuO\cdot(1-x)[3B_2O_3\cdot(1-y)PbO\cdot yAg_2O]$ glass system

Peak positions [cm^{-1}]	**Raman assignments**
~460	isolated diborate groups
~690	metaborate groups
~760	symmetric breathing vibrations of six member borate rings with one or two $BØ_3$ triangle replaced by $BØ_4^-$ tetrahedral
~790	Symm4etric breathing vibrations of boroxol rings
~940 ~1067	diborate groups
~1260	pyroborate groups
~1335 ~1350	$BØ_2O^-$ triangles linked to $BØ_4^-$

For the matrix with y = 0.3 the Raman data reveal a structure similar to that mentioned for the matrix with y = 0.1, although there are changes regarding the relative intensity of some Raman bands. It seems that for a higher content of silver oxide and less lead oxide the linkages between the BØ$_2$O$^-$ triangles and BØ$_4^-$ unit break (the intensity of the band decrease) favoring the formation of BO$_3$ pyroborate groups as reflected by the appearance of the shoulder centered at 1260 cm^{-1}. The intensity of the bands given by the rings containing only BO$_3$ units and the rings with one or two BØ$_3$ triangle replaced by BØ$_4^-$ units attains almost equal Raman intensities for this system. In the glass network, the presence of chained diborate groups is given by a broad envelope coming from the overlapping of the bands centered at 940 and 1067 cm^{-1}.

Comparing both matrices, y =0.1 versus y = 0.3 it can be observed an increase in the depolymerization degree of the network reflected by a drastically decrease in intensity of all the Raman bands, along with the appearance of a new shoulder assigned to the pyroborate groups.

Raman spectra of both matrices y = 0.1 and y = 0.3 gradually doped with copper oxide are present in figure 2, along with the frequencies and their assignments listed in table I.

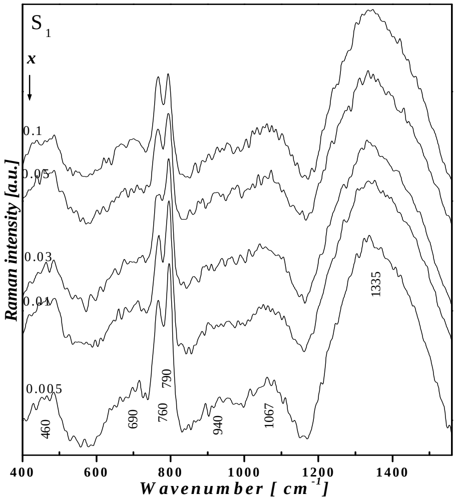

a)

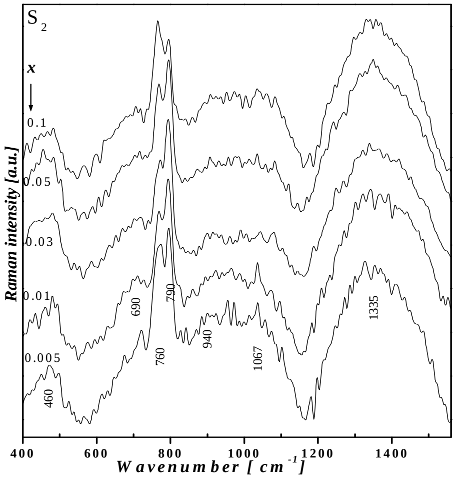

(b)

Fig 2. Raman spectra of xCuO·(1-x)[$3B_2O_3$·(1-y)PbO·yAg_2O] glass system (a) for y = 0.1 and (b) for y = 0.3

Adding gradually copper oxide in the first matrix (S_1), it can be observed that Raman data expose the same bands as those recorded for the system y = 0.1. Only the band characteristic to the $B\O_2O^-$ triangles linked to $B\O_4^-$ exhibits a slight change in the wavenumber position. The shift to a lower wavenumber (1335 cm^{-1}) is due to a distortion or a break in the BO_3 triangle linked to a BO_4 unit. Still, there is a continuous conversion of the BO_3 into BO_4 units, (between the boroxol rings and the rings that contains one or two $B\O_3$ triangle replaced by $B\O_4^-$ units called pentaborate or triborate groups) evidenced by the change in the relative intensity of both bands. In case of the sample with x = 0.1 copper oxide content the intensities of the bands characteristic to the pentaborate or triborate groups and to the boroxol ring attains almost equal Raman intensities. In case of the other Raman bands, there is a continuous decrease in the relative intensity for all the compositional range, this behavior indicating a progressive disorder of the network.

Regarding the second matrix (y = 0.3) doped gradually with copper oxide (S_2) the Raman spectra show the same features as in the case of the system (S_1), the man differences could be observed in the relative intensities of the bands. The presence of copper oxide in this system causes a decrease in intensity of the band from 790 cm^{-1} on the expense of the band at 760 cm^{-1}. If in the case of the sample with x = 0.1 (S_1) we have the same intensity for both Raman bands (760 and 790 cm^{-1}); for the S_2

system the intensity of the band centered at 760 cm^{-1} attains a maximum value meaning that there is an increase of the BO_4 units. The bands centered at 940 and 1067 cm^{-1} attributed to the presence of diborate chain groups develop simultaneously on a broad envelope denoting a break in the chains forming more isolated diborate groups. This explains the increase in intensity of the band centered at 460 cm^{-1}. In addition, the number of $BØ_2O^-$ triangles linked to $BØ_4^-$ becomes smaller, behavior reflected by the decrease in intensity of the band centered at 1335 cm^{-1}.

Conclusions

For both matrices y = 0.1 and 0.3, of the system $xCuO\cdot(1-x)[3B_2O_3\cdot(1-y)PbO\cdot yAg_2O]$ the Raman data reveal only the presence of borate groups such as: boroxol rings, diborate, pyroborate and metaborate groups. Increasing the Ag_2O/PbO ratio implies an increase in the depolimerization degree of the network structure exposed by a general decrease in intensity of the Raman bands.

With the controlled addition of copper oxide in both matrices, the intensity of the characteristic boroxol ring peak (790 cm^{-1}) decreases, quite the reverse with peak at 760 cm^{-1}. The variation in the relative intensities of the two peaks corresponds to the conversion of BO_3 into BO_4 units. In addition, there is a continuous decrease in intensity of the borate Raman bands denoting for both systems a progressively disorder of the vitreous network. Still, no vibrational modes corresponding to Ag_2O, PbO or CuO were evidenced.

REFERENCES

1. A. A. Ahmed, M. R. El-Tohamy, Glass Tecnol. **38** (3), 97 (1997)
2. W. A. Pisarski, J. Pisarsk, W. Ryba-Romanowski, J. Mol. Struct. **744–747**, 515 (2005)
3. M. Ganguli, K. J. Rao, J. Solid State Chemistry **145**, 65 (1999)
4. Z. Pan, S. H. Morgan, B. H. Long, J. Non-Cryst. Solids **185**, 127 (1995)
5. A. Tawansi, I. A. Gohar, D. Holland, N. A. El-Shishtawi, J. Phys. D: Appl. Phys. **21**, 607 (1988)
6. E. Burzo, I. Ardelean, Phys. Chem. Glasses, **20 (1)**, 15 (1979)
7. T. Takaishi, J. Jin, M Takaishi, T. Uchino, T. Yoko, Proc. Int. Congr. Glass. Volume 2. Extended Abstracts, Edinburgh. Scotland, 1-6 July 2001
8. O. Sipr, G. Dalba, F. Rocca, Phys. Rev. B **69**, 134201 (2004)
9. C. P. Varsamis, E. I. Kamitsos, G. D. Chryssikos, Solid State Ionics **136–137,** 1031 (2000)
10. M. Cutroni, M. Federico, A. Mandanici, P. Mustarelli, C. Tomasi, Solid State Ionics **113–115**, 681 (1998)

11. J. A. Duffy, B. Harris, E. I. Kamitsos, G. D. Chryssikos, J. A. Kapoutsis, Phys. Chem. Glasses **39** (5), 275 (1998)
12. M. Soliman Selim, E. Metwalli, Materials Chemistry and Physics **78**, 94 (2002)
13. R. Ciceo Lucacel, C. Marcus, V. Timar, I. Ardelean, submitted at J. Optoelectron. Adv. Mat. (2006)
14. A. O. Hulpus, J. Monteiro, S. K. Mendiratta, M. F. Carrasco, I. Ardelean, J. Non-Cryst. Solids **352**, 1495 (2006)
15. E. Burzo, I. Ardelean, I. Ursu, J. Mat. Sci. **15**, 581 (1980)
16. H. Doweidar, K. El-Igili, S. Abd El-Maksoud, J. Phys. D: Appl. Phys. **33**, 2535 (2000)
17. I. Ardelean, A. O. Hulpus, R. Ciceo-Lucăcel, International Conference „ADVANCED SPECTROSCOPIES on BIOMEDICAL and NANOSTRUCTURED SYSTEMS” (NanoSpec), 3-6 september 2006, Cluj-Napoca, Romania, submitted for publication at J. Optoelectron. Adv. Mat. (2006)

STUDIA UNIVERSITATIS BABEŞ-BOLYAI, PHYSICA, LI, 2, 2006

MAGNETISM AND X-RAY PHOTOELECTRON SPECTROSCOPY OF $AlNi_{1-x}Mn_x$ ALLOYS

**V. REDNIC[1], R. PACURARIU[1], L. REDNIC[1], V. POP[1],
M. NEUMANN[2], M. COLDEA[1]**

ABSTRACT. The electronic and magnetic properties of the two alloys $AlNi_{0.4}Mn_{0.6}$ and $AlNi_{0.5}Mn_{0.5}$ belonging to $AlNi_{1-x}Mn_x$ system, obtained from X–ray photoelectron spectroscopy and magnetic measurements, are reported. The most important feature of the XPS spectra is the well-defined magnetic exchange splitting of about 5 eV of the Mn *3s* core levels of both alloys, arising from the exchange interactions between the core hole and open *3d* shell. This gives a clear evidence of the existence of local moments in the Anderson's sense, confined on Mn sites in these alloys. For both alloys the Mn and Ni *3d* bands are filled more than half, which leads to a ferromagnetic coupling between the neighbouring local magnetic moments situated at Mn and Ni sites. By correlating the information from the XPS core levels spectra and magnetic measurements in the ordered and paramagnetic states, the magnetic behaviour of $AlNi_{0.4}Mn_{0.6}$ and $AlNi_{0.5}Mn_{0.5}$ can not be explained in the picture of ferromagnetic systems with a collinear arrangement of the local magnetic moments. We propose a canted ferromagnetism in the two alloys, which should be verified by further neutron diffraction investigations.

Keywords: Transition metal alloys and compounds; Magnetic measurements; XPS spectra; Local moments

1. Introduction

The problem of local moments confined to the transition metals sites, i.e., localized behaviour in some aspects of itinerant electrons, is one of the most important issues in the physics of the magnetic alloys and intermetallic compounds [1]. It is already known that Mn-based Heusler alloys have a magnetic moment of about $\mu \approx 2.5\mu_B$-$4\mu_B$ localized at the Mn site [2]. Traditionally they are considered as ideal systems with local magnetic moments. In the phase diagram of the Al-Mn-Ni system there are three regions of solid solubility and a Heusler alloy: Ni_2MnAl. Some of the Al-Mn-Ni alloys are potential candidates to exhibit giant magnetic field induced strains [3]. The aim of this paper is to study the effects of substitution of Ni for Mn in AlNi which is a Pauli paramagnet [4].We discuss the electronic and magnetic properties of $AlNi_{0.4}Mn_{0.6}$ and $AlNi_{0.5}Mn_{0.5}$ alloys, obtained from X–ray photoelectron spectroscopy and magnetic measurements.

---

[1] Babes-Bolyai University, Faculty of Physics, 400084 Cluj-Napoca, Romania
[2] University of Osnabrück, Fachbereich Physik, 49069 Osnabrück, Germany

2. Experimental

Polycrystalline samples were prepared by arc melting technique in a cold copper crucible under an argon atmosphere. The purity of the starting materials was 99.999% for Al, 99.99% for Mn and 99.9% in case of Ni. The weight loss of the final material was found to be less than 1 %. The homogeneity of the samples was checked by conventional X-ray powder diffraction with Cu K_α radiation, using a *Bruker D8 Advance* powder diffractometer. X-ray diffraction patterns show the presence of a single phase for each sample. Fig.1 shows the XRD pattern for one alloy compared with the theoretical diffractogram of AlNi.

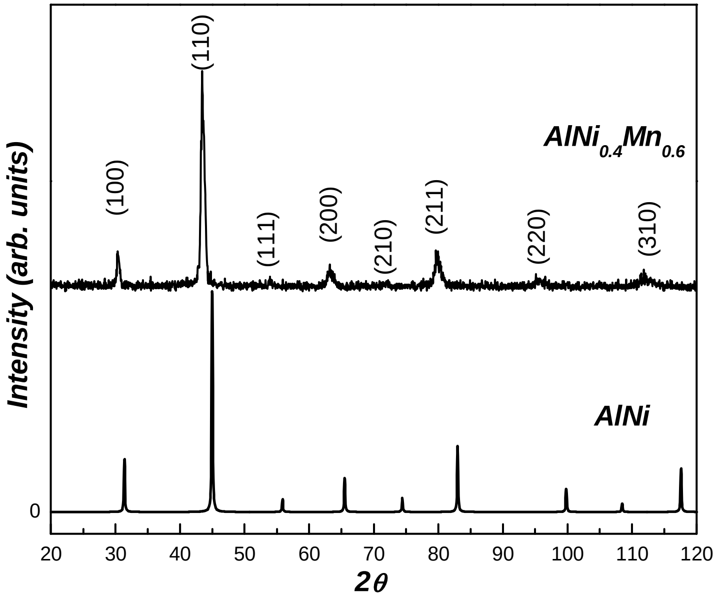

Fig. 1. X-ray diffraction pattern of $AlNi_{0.4}Mn_{0.6}$ compared to AlNi

The two alloys have the same crystalline structure as the parent compound AlNi (bcc-ClCs), with slightly different lattice parameters: a=2.953 Å for $AlNi_{0.5}Mn_{0.5}$ and a=2.937 Å for $AlNi_{0.4}Mn_{0.6}$ (a=2.848 Å for AlNi [5]). Our performed Rietveld analysis indicate that Mn and Ni atoms occupy the 1(b) positions, having in their first vicinity eight Al atoms situated at the 1(a) positions, as shown in Fig. 2.

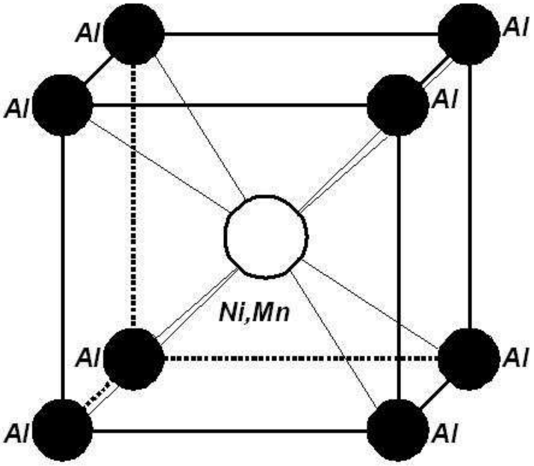

Fig. 2. Schematically representation of the elementary cell of $AlNi_{1-x}Mn_x$

The magnetic measurements were performed using a vibrating magnetometer in the temperature range 4.2 – 850K and fields up to 90 kOe. The XPS spectra were recorded using a PHI 5600ci ESCA spectrometer with monocromatized AlK_α radiation at room temperature. The pressure in the ultra-high vacuum chamber was in the 10^{-10} mbar range during the measurements. The samples were crushed in situ. The surface cleanness was checked by monitoring the oxygen and carbon 1s levels.

3. Results and Discussions

3.1. Magnetic measurements

The temperature dependence of the spontaneous magnetization and of the reciprocal susceptibility of $AlNi_{0.4}Mn_{0.6}$ and $AlNi_{0.5}Mn_{0.5}$ are shown in Figs. 3 and 4, respectively.The values and variations of magnetization of $AlNi_{0.4}Mn_{0.6}$ and $AlNi_{0.5}Mn_{0.5}$ with magnetic field and temperature suggest that both alloys have a ferromagnetic behaviour below the Curie temperatures 385K and respectively 401K, determined from the usual Arrot plots. The spontaneous magnetizations extrapolated to 0K have the values 0.765 μ_B/f.u. for $AlNi_{0.5}Mn_{0.5}$ and 1 μ_B/f.u. for $AlNi_{0.4}Mn_{0.6}$.

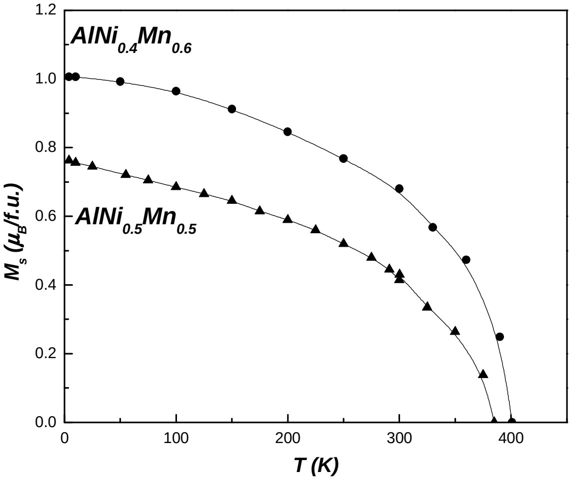

Fig. 3. Thermal variation of the spontaneous magnetization of $AlNi_{0.4}Mn_{0.6}$ and $AlNi_{0.5}Mn_{0.5}$

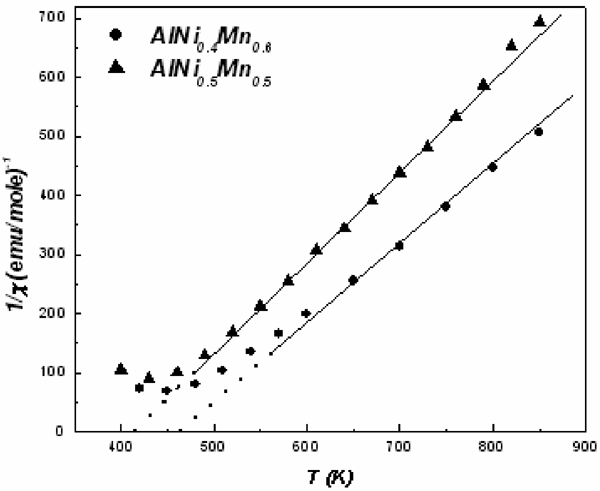

Fig. 4. Thermal variation of the reciprocal susceptibility of $AlNi_{0.4}Mn_{0.6}$ and $AlNi_{0.5}Mn_{0.5}$

In the temperature range 300-900K, the magnetic susceptibilities obey the Curie-Weiss law, $\chi = C / (T-\theta)$, with the paramagnetic Curie temperatures $\theta = 411K$ for $AlNi_{0.5}Mn_{0.5}$ and $\theta = 460K$ for $AlNi_{0.4}Mn_{0.6}$. The effective magnetic moments, determined from the Curie constants, have the values 2.29 μ_B/f.u. and 2.47 μ_B/f.u. for $AlNi_{0.5}Mn_{0.5}$ and $AlNi_{0.4}Mn_{0.6}$, respectively.

3.2 XPS spectra

The electronic structure of the two alloys is studied by analyzing the valence band and core level spectra.

The Mn 3s spectra for $AlNi_{0.4}Mn_{0.6}$ and $AlNi_{0.5}Mn_{0.5}$ are shown in Fig. 5. Both spectra exhibit a well-defined magnetic exchange splitting of about 5 eV, arising from the exchange interactions between the *3s* core hole and open *3d* shell [6]. This gives a clear evidence of the existence of local moments in the Anderson's sense confined on Mn sites in the studied alloys [7]. The magnitude of the 3s spectral splitting according to the Van Vleck theorem [8] is determined by:

$$\Delta E_{ex} = \frac{1}{2l+1}(2S+1)G^2(3s,3d),$$

where S is the total spin of the ground state of the *3d* electrons, l is the orbital quantum number and $G^2(3s,3d)$ is the Slater exchange integral. The energy separation is proportional to the total spin of the ground state of the *3d* electrons, and hence it can be used to estimate the magnetic moment due to unpaired *3d* electron spins in the solid.

The fitting of the Mn *3s* spectra with two exchange components and a Shirley background [9] is presented in Fig. 5. We found a separation value of 5.1 eV in $AlNi_{0.5}Mn_{0.5}$ and 5 eV in $AlNi_{0.4}Mn_{0.6}$, which correspond to a magnetic moment of about 3 μ_B /Mn in an ionic model [10].

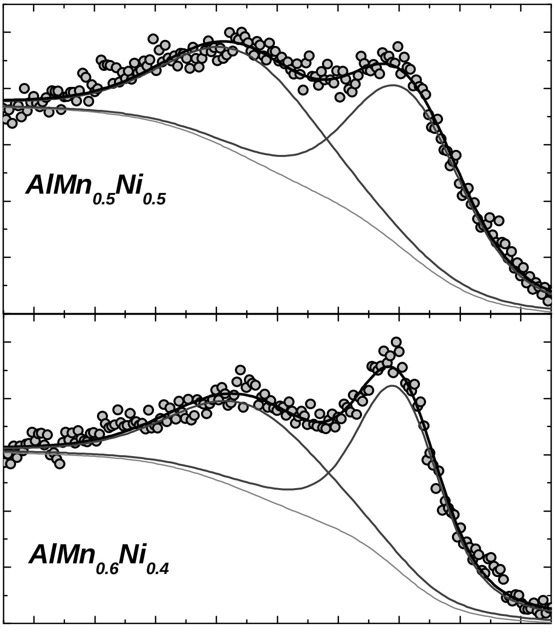

Fig. 5. XPS Mn 3s core level spectra of $AlNi_{0.4}Mn_{0.6}$ and $AlNi_{0.5}Mn_{0.5}$

In Fig. 6 are shown the Ni *2p* core level spectra of $AlNi_{0.4}Mn_{0.6}$ and $AlNi_{0.5}Mn_{0.5}$ in comparison to pure metallic Ni.

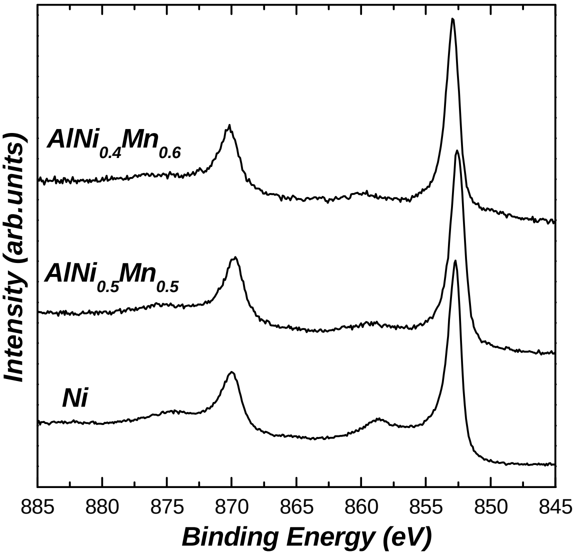

Fig. 6. XPS Ni 2p core level spectra of $AlNi_{0.4}Mn_{0.6}$ and $AlNi_{0.5}Mn_{0.5}$and metallic Ni

The presence of satellites in the Ni *2p* core level spectra of $AlNi_{0.4}Mn_{0.6}$ and $AlNi_{0.5}Mn_{0.5}$, at ~6 eV higher binding energy than the main line, implies the presence of *d* character in the unoccupied bands. By comparing the Ni *2p* core level spectra of $AlNi_{0.4}Mn_{0.6}$ and $AlNi_{0.5}Mn_{0.5}$ to the one of metallic Ni, a decrease in Ni satellite intensity can be observed, which is attributed to the partial filling of the Ni *3d* band. The intensities of the Ni satellites are known to be proportional to the number of holes in the Ni *d* band [11]. After fitting the *2p* core level spectra and considering a number of 0.6 holes per Ni atom for metallic Ni, we estimated ~0.3 holes per Ni atom for both alloys. The partial filling of the Mn *3d* and Ni *3d* states, indicated by the XPS core level spectra, is attributed to the hybridization of the Al states with Mn and Ni states.

The XPS valence-band spectra for the two alloys are shown in Fig. 7:

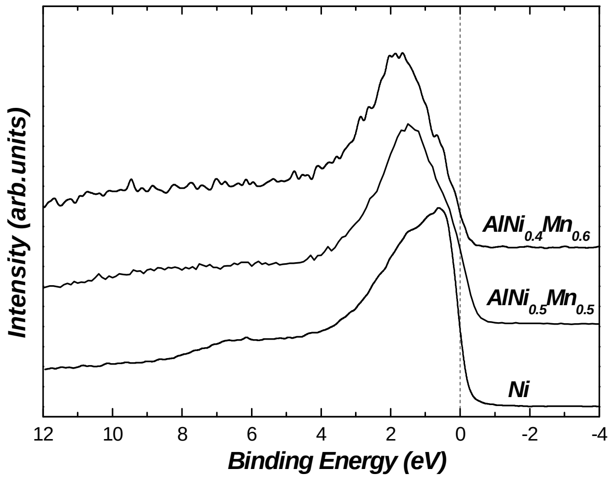

Fig. 7. XPS valence-band spectra of $AlNi_{0.4}Mn_{0.6}$ and $AlNi_{0.5}Mn_{0.5}$

At Al K_α radiation, the Ni *3d* cross section is about four times larger than the Mn *3d* cross section, i.e., the valence-band of $AlNi_{0.4}Mn_{0.6}$ and $AlNi_{0.5}Mn_{0.5}$ are dominated by the Ni *3d* states. The valence band spectra of both alloys exhibit satellites at ~6 eV higher binding energy than the centroid, confirming the presence of *d* character in the unoccupied bands. The substitution of Ni by Mn leads to an increase of the localization of the Ni *3d* electrons, reflected by an energy shift of the valence band maximum to higher binding energies. In *d* – band metals and alloys the *3d* states are shifted gradually to higher binding energy with the increasing of the *d* – state occupancy and consequently a decrease of the density of states at the Fermi level occurs [12].

The XPS core level spectra of $AlNi_{0.4}Mn_{0.6}$ and $AlNi_{0.5}Mn_{0.5}$ indicate a partial filling of the Mn *3d* and Ni *3d* states, attributed to the hybridization of the Al *3sp* states with Mn and Ni *3d* states. For both alloys the Mn and Ni *3d* bands are filled more than half, which leads to a ferromagnetic coupling between the neighbouring local magnetic moments situated at Mn and Ni sites [13]. We cannot correlate the data obtained from the magnetic measurements in the ordered and paramagnetic domains considering a ferromagnetic system with a collinear arrangement of the local magnetic moments. A canted ferromagnetism could explain the magnetic behavior of $AlNi_{0.4}Mn_{0.6}$ and $AlNi_{0.5}Mn_{0.5}$. We have to deal with two different types of interactions, a ferromagnetic Mn-Ni interaction and an antiferromagnetic one between two Mn atoms. If we consider a Mn atom in the centre of one unit cell, the nearest six Mn or Ni atoms (placed in the centre of neighbouring cells), will try to orientate the Mn magnetic moment parallel, in case of Mn-Ni interaction, and antiparallel for Mn-Mn interaction. This competition could tilt the Mn magnetic moment from parallel orientation and lead to a canted ferromagnetism.

4. Conclusions

The substitution of Ni for Mn in AlNi leads to no significant changes in the crystallographic structure, but has significant effects on the magnetic properties and electronic structure of the two investigated alloys. The well-defined magnetic exchange splitting of about 5 eV for the Mn *3s* core levels of $AlNi_{0.4}Mn_{0.6}$ and $AlNi_{0.5}Mn_{0.5}$ gives a clear evidence of the existence of local moments in the Anderson's sense confined on Mn sites in Al-Mn-Ni alloys. The hybridization of the Al states with Mn and Ni states leads to a partial filling of the Mn *3d* and Ni *3d* states, as indicated by the XPS core level and valence band spectra. By correlating the experimental data obtained both from ordered and paramagnetic states correlating, the magnetic behaviour of $AlNi_{0.4}Mn_{0.6}$ and $AlNi_{0.5}Mn_{0.5}$ cannot be explained in the picture of ferromagnetic systems with a collinear arrangement of the local magnetic moments. We propose a canted ferromagnetism in the two alloys, which should be verified by further neutron diffraction investigations.

REFERENCES

1. S. Plogmann, T. Schlathölter, J. Braun, M. Neumann, Yu. M. Zarmoshenko, M. V. Zablonskikh, E. I. Shreder, E. Z. Kurmaev, Phys. Rev. B 60, 6428 (1999).
2. P. J. Webster and K. R. A. Ziebeck, in *Alloys and Compounds of d-Elements with Main Group Elem*ents, Part 2, edited by H. R. J. Wijn, Landolt-Börnstein, New Series, Group III, vol. 19, pp. 75-184 (Springer-Verlag, Berlin 1988)
3. A. Fujita, K. Fukamichi, F. Gejima, R. Kainuma, and K. Ishida, *Appl. Phys. Lett*. 77, 3054 (2000)
4. Ch. Müller, H. Wonn, W. Blau, P. Ziesche, V.P. Krivitskii, Phys. Stat. Sol. (b) 95 (1979) 215
5. M. Nastasi, L. S. Hung, H. H. Johnson, J. W. Mayer and J. M. Williams, J. Appl. Phys., New York, 57 (4), 1050-1054 (1985)
6. C.S. Fadley, D. A. Shirley, A. J. Freeman, P. S. Bagus, and J. V. Mallow, *Phys. Rev. Lett*. 23, 1397 (1969)
7. P. W. Anderson, *Phys. Rev*. 124, 41 (1961)
8. J. H. Van Vleck, *Phys. Rev*. 45, 405 (1934)
9. D. A. Shirley, *Phys. Rev*. B 5, 4709 (1972)
10. V. R. Galakhov, M. Demeter, S. Bartkowski, M. Neumann, N. A. Ovechkina, E. Z. Kurmaev, N. I. Lobachevskaya, Ya. M. Mukovskii, J. Mitchell, D. L. Ederer, *Phys. Rev*. B 65, 113102 (2002)
11. J.C. Fuggle and Z. Zolnierek, *Solid State Commun.* 38, 799 (1981)
12. P. Steiner, H. Hochst, S. Hufner, *J. Phys.* F 7, L105 (1977)
13. T. Moriya, *Solid State Commun*. 2, 239 (1964)

STUDIA UNIVERSITATIS BABEŞ-BOLYAI, PHYSICA, LI, 2, 2006

OPERATING STABILITY DIAGRAM FOR THE PLASMA NEEDLE

ALPÁR SIMON*, SORIN DAN ANGHEL

ABSTRACT. This paper presents the operating stability diagram for atmospheric pressure non-thermal He plasma, known as “the plasma needle”. The data necessary for plotting such a diagram were obtained by performing visual observations on the plasma ignition, formation and aspect as function of gas flow-rate at different RF plasma powers. The spatial dimensions of the plasma and its mechanical behavior were also monitored.

1. Introduction

The interest on non-thermal atmospheric pressure plasmas is in continuous increasing due to their applications in medicine, biology, technology and material science. The most important applications to mention are: sterilization [1], high precision cellular removal [2] (in surgery and oncology), plasma display panels and plasma surface treatments of various heat sensitive materials (polymers, plants, fabric). Non-thermal plasmas at atmospheric pressure could be obtained using almost the same experimental conditions as for the hotter plasmas ($T_{gas} \sim 10^2 - 10^3$ K) but some very important aspects have to be considered: plasma gas flow-rates and operating voltages has to be reduced; the plasma volume has to be kept as small as possible.

The “plasma needle” is one of the newest non-thermal plasma with very promising biomedical applications [3 – 6]. It could be obtained at atmospheric pressure, in He gas flow (Ar, N_2, He and air mixtures may be used too), around a sharp metallic electrode, with RF frequencies around 13.56 MHz. Its main characteristic is that it is non destructive for living cells, it is obtained at room temperature and has a small penetration depth [7]. It is a source of charged particles, soft UV radiation and active oxygen radicals and it is studied extensively in many laboratories from both experimental [8 – 12] and theoretical point of views [13 – 14].

The “plasma needle” type discharge was obtained successfully in our laboratory, at atmospheric pressure in He flow, at both 1 MHz and 10 MHz, with RF power levels below 5 W. Some preliminary results regarding generation and some physical characteristics were already published [15].

The aim of this paper is to obtain an operating stability diagram for the plasma needle and to establish the optimum working parameters for this device.

---

* "Babeş-Bolyai" University, Faculty of Physics, M. Kogalniceanu 1, 400084 Cluj, Romania
E-mail: asimon@phys.ubbcluj.ro; anghels@phys.ubbcluj.ro

2. Experimental

The plasma needle was generated using an RF oscillator described elsewhere [16]. As compared to the experimental set-up used by other authors to generate the plasma needle, we have exploited the possibility of obtaining various RF voltages from the resonant circuit of the free running type RF oscillator. The maximum RF power could be achieved easily by adjusting the coupling factor between the oscillating circuit's coil and the reaction coil.

The schematic diagram of the needle is presented in Fig.1. The RF power is transmitted from the generator towards the needle directly, via a BNC connector.

This torch is a simplified version of that presented and described earlier [15]. No coaxial cable is used to connect the torch to the RF generator, therefore extra losses due to radiation and dissipation are substantially reduced. The experimental set-up is presented schematically in Fig.2.

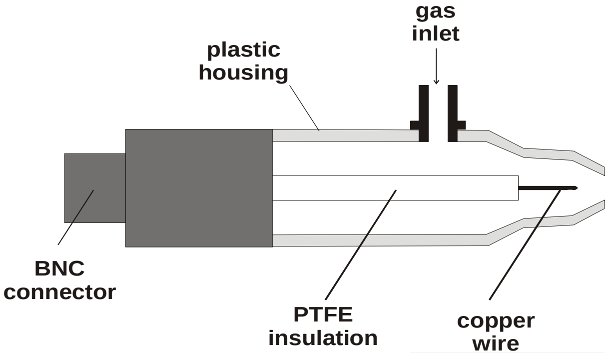

Fig.1 The plasma needle configuration

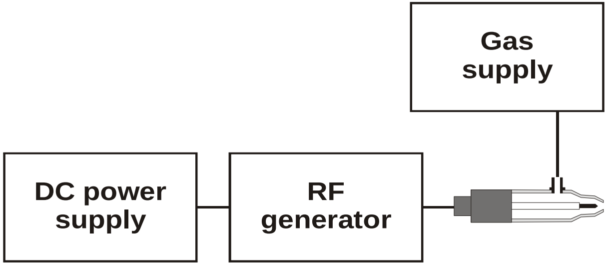

Fig.2 The experimental set-up

The operating stability diagram is obtained by following step-by-step the procedure described by Rezaaiyaan *et al.* [17], Forbes *et al.* [18] and Spencer *et al.* [19].

The data necessary for plotting such a diagram are obtained by performing visual observations on plasma formation and aspect, as function of gas flow-rate (0 to 6 l/min) at different RF plasma powers.

The spatial dimensions of the plasma and its mechanical behaviour have to be monitored, too.

The plasma power was estimated using the subtraction methodology suggested by Horowitz [20]: the absorbed RF power by the plasma is equal to the difference between the transmitted power from the generator in the presence and absence of the discharge, at the same d.c. supply voltage (E_A): $P_{plasma} = E_A (I_{Ap} - I_{Ao})$, where I_{Ap} and I_{Ao} represents the supply current intensities in the presence and absence of the plasma.

3. Results and Discussions

The operating stability diagram presented in Fig.3 indicates that as function of supply voltage and plasma gas flow-rate there are three different shapes for the plasma.

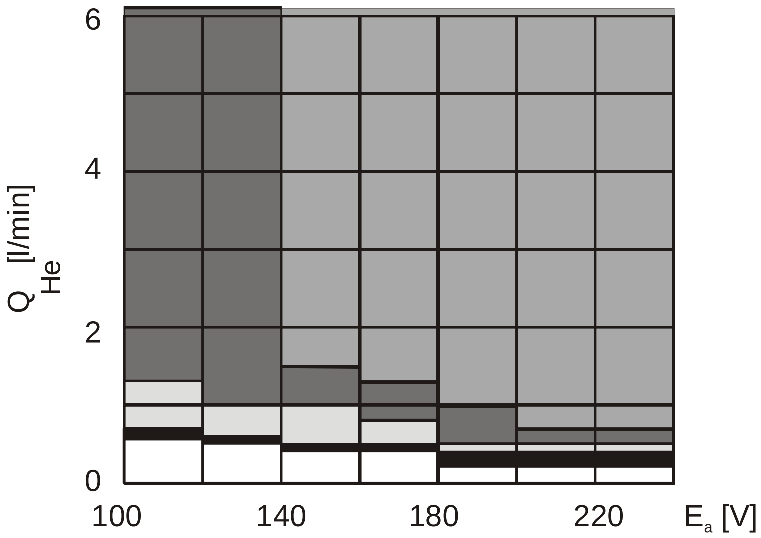

Fig.3 Operating stability diagram for the plasma needle

□ - no plasma; ■ - very small, point-like plasma (0.5 mm in diameter);

▒ - ball shaped plasma (1 mm in diameter); ▓ - ball shaped plasma (2 mm in diameter);

▨ - ellipsoidal shaped plasma (3 mm in diameter, length depending on the gas-flow rate)

Thus, the region denoted “*no plasma*” is defined by He flow-rates below 0.5 l/min for lower d.c. supply voltage levels (100 – 140 V), 0.4 l/min for medium voltages (140 – 180 V) and around 0.2 l/min for higher voltages (from 180 V to 220 V).

The region colored in black on the stability diagram and denoted “*point-like*” plasma defines the operating conditions at which the discharge is ignited, the resulting plasma being very small (luminous ball, around 0.5 mm in diameter).

The increase of the flow-rate or of the d.c. supply voltage determines a development of the plasma and its transformation into a ball shaped discharge. At lower flow-rates (below or around 1 l/min) it has a diameter around 1 mm.

For higher d.c. supply voltages (over 180 V) or for high flow-rates (over 1.3 l/min, but voltages below 140 V) the plasma increases its volume, becoming a well formed plasma-ball with a diameter around 2 mm.

The region denoted “*ellipsoidal shaped plasma*” is defined exclusively by supply voltages higher than 140 V (up to 200 V) and He flow-rates from 1.0 – 1.5 l/min to 6 l/min or by higher voltages (220 – 240 V) and a wider flow interval (0.7 – 6.0 l/min). It has to be mentioned that for this region that by increasing the He flow-rate the plasma ellipsoid length will increase from 3 mm up to 6 mm.

The plasma power as function of He flow-rate for different supply voltages is presented in Fig.4.

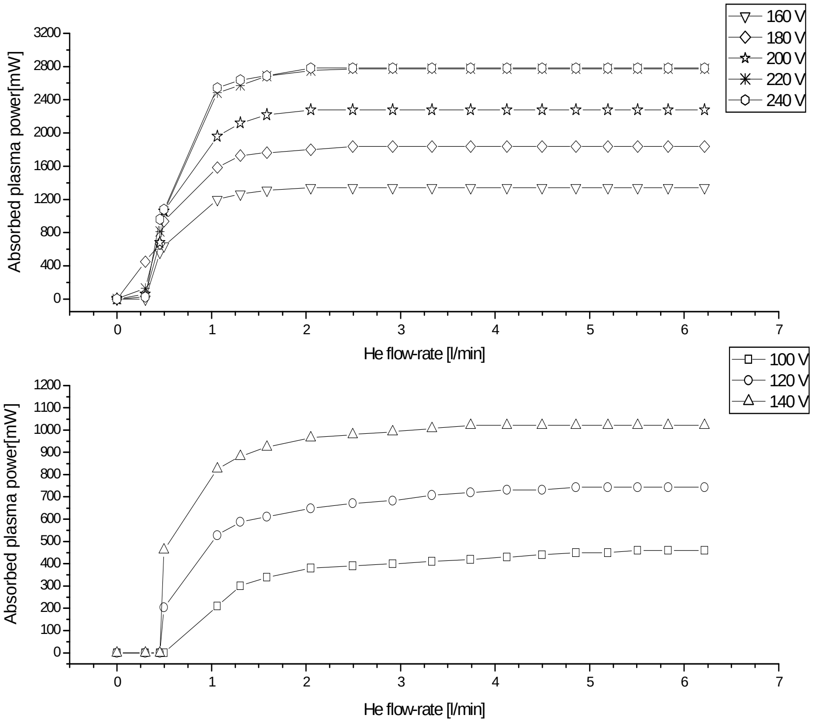

Fig.4 Plasma power as function of He flow-rate for different supply voltages

As can be seen, the plots are in agreement with the stability diagram. All the plots are showing that the plasma is well formed at starting flow-rate of 0.5 l/min and the presence of a saturation tendency is suggested starting from 1.0 – 1.5 l/min (the plasma becomes fully developed). To take into account the increased plasma volume, the plasma power density was calculated too. Its tendency, as function of He flow-rate, supports the above presented findings. The plasma power, the plasma volume and the plasma power density as function of He flow-rate are presented in Fig.5 for E_A = 100 V and 220 V.

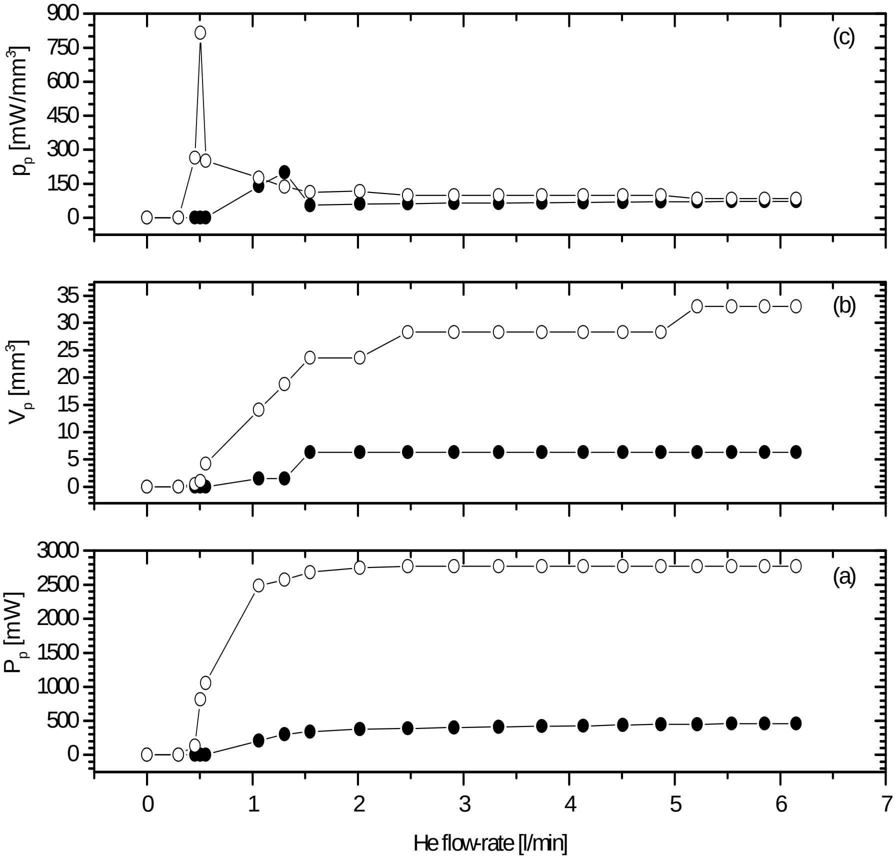

Fig.5. Plasma power P_p (a), plasma volume P_V (b) and plasma power density p_p (c) as function of He flow-rate for 100 V (●) and 220 V (○)

The plasma power density is increasing around 1.25 l/min at 100 V and 0.5 l/min for all the other supply voltages, after that decreasing simultaneously with the increase of the gas flow-rate (plasma power saturated, volume increased).

4. Conclusions

The operating stability diagram for an atmospheric pressure He plasma needle was obtained and it indicates that as function of supply voltage and plasma gas flow-rate there are three different shapes for the plasma. Using this diagram the optimum working parameters could be established for the atmospheric pressure He plasma needle as function of the specific requirements of the performed studies and applications.

This work was supported by the Romanian Ministry of Education through National Authority for Scientific Research RTD National Programme CEEX under Grant ET 99 (5858 / 2006).

REFERENCES

1. M. Laroussi, I. Alexeff, J.P. Richardson and F.F. Dier, *IEEE Trans. Plasma Sci.* **30,** 158 – 159 (2002)
2. E. Stoffels, A.J. Flikweert, W.W. Stoffels and G.M.W. Kroesen, *Plasma Sources Sci. Technol.* **11**, 383 – 388 (2002)
3. I.E. Kieft, K. Douma , R.T.A. Megens, M.A.M.J. van Zandvoort , D.W. Slaaf, E. Stoffels: "*Non-thermal plasma treatment of ex vivo arteries: preliminary results*" – presented at XXVIIth ICPIG, Eindhoven, the Netherlands, 18-22 July, 2005
4. D. Borg, P. Henley, A. Husain, N. Stroeher, P. King, E. Stoffels: "*Development of a Gas Plasma Catheter for Gas Plasma Surgery*" – presented at XXVIIth ICPIG, Eindhoven, the Netherlands, 18-22 July, 2005
5. L.J.M. van den Bedem, R.E.J. Sladek, M. Steinbuch, E. Stoffels Adamowicz: "*Plasma treatment of S. mutans biofilms cultured in a simulated dental cavity model*" – presented at XXVIIth ICPIG, Eindhoven, the Netherlands, 18-22 July, 2005
6. R.E.J. Sladek, E. Stoffels, R. Walraven, P.J. Tielbeek and R.A. Koolhoven, *IEEE Trans. Plasma Sci.* 32, 1540 – 1543 (2004)
7. E. Stoffels, *High Temp. Material Processes* **6**, 191 – 202 (2002)
8. I.E. Kieft, E.P. v.d. Laan and E. Stoffels, *New Journal of Physics* **6** (149), 1 - 14 (2004)
9. R.E.J. Sladek and E. Stoffels, *J. Phys. D: Appl. Phys.* **38**, 1716 – 1721 (2005)
10. N. Puac, Z. Lj. Petrovic, G. Malovic, A. Dordevic, S. Zivkovic, Z. Giba and D. Grubisic, *J. Phys. D: Appl. Phys.* **39**, 3514 – 3519 (2006)
11. J. Goree, B. Liu and D. Drake, *J. Phys. D: Appl. Phys.* ***39***, 3479 – 3486 (2006)
12. E. Stoffels, I.E. Kieft, R.E.J. Sladek, L.J.M. v.d. Bedem, E.P. v.d. Laan and M. Steinbuch, *Plasma Sources Sci. Technol.* **15**, S169 – S180 (2006)

13. Y. Sakiyama and D.B. Graves, *J. Phys. D: Appl. Phys.* ***39***, 3451 – 3456 (2006)
14. Y. Sakiyama and D.B. Graves, *J. Phys. D: Appl. Phys.* ***39***, 3644 – 3652 (2006)
15. S.D. Anghel, A. Simon and E. Hainal-Filla, *Studia seria Physica* **L**, 51 – 56 (2005)
16. S.D. Anghel, *IEEE Trans. Plasma Sci.* **30**, 660 (2002)
17. R. Rezaaiyaan, G.M. Hieftje, H. Anderson, H. Kaiser and B. Meddings, *Appl. Spectrosc.* **36**, 627 – 631 (1982)
18. K.A. Forbes, E.E. Reszke, P.C. Uden and R.M. Barnes, *J. Anal. At. Spectrom* **6**, 57 – 71 (1991)
19. B.M. Spencer, B.W. Smith and J.D. Winefordner, *Appl. Spectrosc.* **48**, 289 – 296 (1994)
20. Ch.M. Horowitz, *J. Vac. Sci. Technol. A* **1** (14), 1785 – 1800 (1983)

STUDIA UNIVERSITATIS BABEŞ-BOLYAI, PHYSICA, LI, 2, 2006

SPECTROSCOPIC AND MAGNETIC INVESTIGATION OF TETRANUCLEAR Mn(II) CLUSTER ENCAPSULATED IN SANDWICH-TYPE HETEROPOLYANION

M. HOSSU[1], D. RUSU[2], M. RUSU[3], A. MARCU[1], L. DAVID[1]

ABSTRACT. The sandwich-type $Na_{10}[Mn_4(H_2O)_2(AsW_9O_{34})_2]\cdot 27H_2O$ complex was prepared and investigated through spectroscopic (FT-IR, UV-VIS, ESR) methods and magnetic susceptibility measurements.

The analysis of the co-ordination mode of transition metal ions was made by means comparison between the FT-IR spectra of the sandwich-type complex with those of $Na_9[AsW_9O_{34}]\cdot 11H_2O$ ligand. The relatively small shift (9 cm^{-1}) of the $\upsilon_{asym}(W{=}O_t)$ vibration band is due to the fact the terminal O_t atoms are not involved in the co-ordination. The opposite shift of $\upsilon_{asym}(W\text{-}O_e\text{-}W)$ and $\upsilon_{asym}(W\text{-}O_c\text{-}W)$ frequencies for the bandings from the belt region shows the co-ordination of each metallic ion at these oxygen atoms.

The more intense band in the UV spectra corresponding to the $p_\pi(O_t) \rightarrow d_{\pi^*}(W)$ transitions is centred at 49100 cm^{-1} and 49300 cm^{-1} for ligand and complex respectively. This is in agreement with the co-ordination of the Mn (II) ions in the lacunary region of the ligand and not to the terminal oxygen atoms. The broader band centred at 39732 cm^{-1} in the ligand spectrum belongs to the $p_\pi(O_{c,e}) \rightarrow d_{\pi^*}(W)$ change transfer transition in the tricentric bonds. This band is shifted towards lower energies in the case of the complex (at 39467 cm^{-1}).

The Gaussian deconvolution of the visible spectrum shows the presence of a band centered at 29340 cm^{-1} assigned to the $^6A_{1g}(S) \rightarrow {}^4E_g(D)$ transition of the Mn^{II} ions in O_h distorted symmetry.

The value of the effective magnetic moment $\mu_{eff} = 11.81\mu_B$ corresponds to an S = 5 spin state. The EPR spectrum of the complex obtained at room temperature indicate the presence of antiferromagnetic coupling between the Mn(II) ions.

1. Introduction

Sandwich-type heteropolyoxometalates (HPOM) in which 3d transition metal ions link two trivacant Keggin fragments are intensely studied for their applications in catalysis, medicine and material science [1-4]. The interaction between the transition ions depends on their type and the geometry of the metallic cluster.

For example, four Cu^{II}, Fe^{III} or Mn^{II} ions are antiferromagnetically coupled in complexes with phosphorous as heteroatom [5], while the Ni^{II} ions usually interact ferromagnetically [6-7].

---

[1] “Babes-Bolyai” Univ., Dept. of Physics, Cluj-Napoca, Romania
[2] “Iuliu Hatieganu” Med. and Pharm. Univ., Dept. of Chem.-Phys., Cluj-Napoca,Romania
[3] “Babes-Bolyai” Univ., Dept. of Chem., Cluj-Napoca, Romania

In order to establish the behavior of transition metals encapsulated in heteropolyoxometalates with As^V as heteroatom, the coordination mode of the metallic ions to the Keggin fragments, the local symmetry around them and the type of metal-metal interactions, the $Na_{10}[Mn_4(H_2O)_2(AsW_9O_{34})_2]\cdot27H_2O$ complex (Fig. 1) was investigated by means of spectroscopic (FT-IR, Vis, EPR) methods methods and magnetic susceptibility measurements. This complex contains two trilacunary Keggin fragments linked by a centrosymmetric rhomb-like Mn_4O_{16} unit, formed by four edge-sharing MnO_6 octahedra [5].

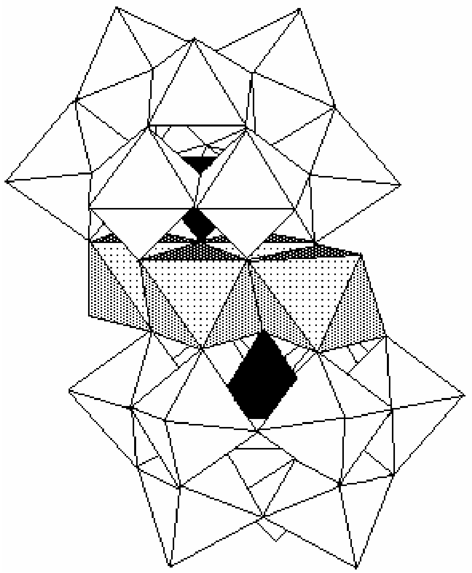

Fig. 1. The structure of the $[Mn_4(H_2O)_2(AsW_9O_{34})_2]^{10-}$ heteropolyanion (Empty polyhedra are WO_6 octahedra, the black triangles are AsO_4 tetrahedra and the shaded units are MnO_6 octahedra).

2. Experimental

The ligand was synthesised according to the procedure described in the reference [8].

Synthesis of the $Na_{10}[Mn_4(H_2O)_2(AsW_9O_{34})_2]\cdot 27H_2O$ complex.

5.36 g (2 mmol) $Na_8[HAsW_9O_{34}]\cdot11H_2O$ was dissolved in 15 mL of distilled water at 70 ^{0}C. After complete dissolution of the salt, 0.98 g (4 mmol) of $Mn(CH_3CO_2)_2\cdot4H_2O$ in 10 ml of distilled water was slowely added with sirring. The mixture was heated to 70 °C for 15 min. The resulting yellow-orange solution (pH = 6.8) was filtered through a sintered-glass frit and allowed to cool at room temperature. After seven days yellow-orange poweder was obtained by filtration and washed with NaCl 2 M, ethanol and ether. The powder was allowed to crystallize after dissolution in hot water (450 mg/5mL). After six days, yellow-orange microcrystals were collected. Yield: 3.91 g (76%). (Found: Na, 4.15; Mn, 3.96; W, 60.08; As, 2.70; H_2O, 8.78. Calcd. for $Na_{10}As_2W_{18}Mn_4O_{142}H_{74}$: Na, 4.17; Mn, 3.98; W, 60.00; As, 2.72; H_2O, 8.81 %).

Physical-Chemical Measurements.

Inductively Coupled Plasma spectroscopy (I.C.P.) was used for the elemental analysis of cerium, lanthanum, arsenic and tungsten and flamephotometry for sodium and potassium.

FT-IR spectra were recorded on a Jasco FT/IR 610 spectrophotometer in the 4000–400 cm^{-1} range, using KBr pellets.

Electronic spectra in the visible range were performed in aqueous solutions on an ATI Unicam-UV-Visible spectrophotometer with Vision Software V 3.20.

EPR spectra on powdered solids were recorded at room (9.617 GHz) and 80 K (9.699 GHz) temperatures in the X-band using a Bruker ESP 380 spectrometer. All g values have been estimated with a $\pm$ 0.002 precision.

3. Results and Discussion

3.1. FT-IR spectra.

New information about the coordination mode of the Mn^{II} ions to the trivacant Keggin fragments have been obtained by comparing the FT-IR spectra of the metallic complex $Na_{10}[Mn_4(H_2O)_2(AsW_9O_{34})_2]\cdot 18H_2O$ and that of the corresponding $Na_9[AsW_9O_{34}]\cdot 11H_2O$ ligand (Table1).

The positions of the bands, their shape and intensity for the complex and for the ligand differ in the 400-1000 cm^{-1} region (Fig. 2).

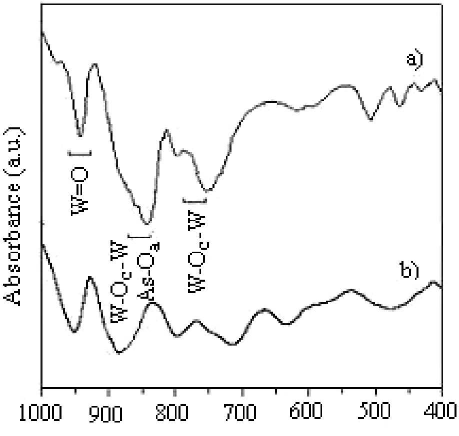

Fig. 2. FT-IR spectra of (a) the ligand and (b) the Mn^{II}–HPOM complex.

The $\nu_{as}(W{=}O_t)$ vibration band for the terminal bonds is unshifted in the FT-IR spectrum of the complex (Table 1) compared to the ligand spectrum because the terminal O_t atoms at the heteropolyoxometalate surface are not involved in the coordination to the Mn^{II} ions.

The vibrational frequency of the As-O bonds found at ~ 820 cm^{-1} overlaps that of W-O_b bonds [8] in both, ligand and complex.

Two vibration bands for the tricentric W–O_e–W bonds of the edge-sharing WO_6 octahedra appear at 877 and 888 cm^{-1} in the FT-IR spectrum of the ligand, suggesting the presence of nonequivalent bonds of this type in the polar and equatorial region of the Keggin fragments (Table 1) [9]. The complex FT-IR spectrum shows a single vibration band at 878 cm^{-1}. The situation changes for the tricentric W–O_c–W bonds of the corner-sharing WO_6 octahedra, with two vibrations in the ligand FT-IR spectrum at 721 and 746 cm^{-1} and three vibrations in the complex spectrum at 709, 743 and 801 cm^{-1}. This behavior of the stretching vibrations of the trinuclear bonds arises from the coordination of the Mn^{II} ions to oxygen atoms from the lacunary region of the ligand [10].

The water molecules present a very broad band with two shoulders for the $\nu_{as}(OH)$ vibrations (Table 1), which indicates the coexistence of crystallization and coordinated water molecules [11]. One of the stretching vibrations of the water molecules, situated at 3250 cm^{-1} in the ligand FT-IR spectrum is significantly shifted at 3185 cm^{-1} in the complex spectrum, which indicate the presence of water molecules directly coordinated to the Mn^{II} ions.

Table 1.

FT-IR data (cm^{-1}) for the ligand and Mn^{II}–HPOM complex[a,b]

Band	Ligand	Complex
$\nu_{as}(W–O_i)$	621 m,sh; 654 m,sh	626 m,b
$\nu_{as}(W–O_c–W)$	721 s,b; 746 s,sh	709 s,b; 743 s,sh; 801 m,b
$\nu_{as}(As–O_i)$	839 m,sh	836 m,sh
$\nu_{as}(W–O_e–W)$	877 s,sp; 888 s,sh	878 s,sp
$\nu_{as}(W{=}O_t)$	943 s,sp	943 s,sp
$\delta(H_2O)$	1616 m,sp	1627 m,sp
$\nu_{as}(OH)$	3250 m,sh; 3420 s,vb; 3505 m,sh;	3185 s,sh; 3404 s,b; 3527 s,sh

[a] O_i is the oxygen which links the As and W atoms, $O_{c,e}$ connect corner and edge-sharing octahedra, respectively, O_t is a terminal oxygen

[b] m–medium, s–strong, sh–shoulder, b–broad, sp–sharp, vb–very broad

3.2. Electronic spectra.

The UV electronic spectra of the sandwich-type complex and of the ligand (Fig. 3) contain two bands characteristic for the ligand to metal change transfer in the heteropolyoxometalates frame. The more intense band corresponding to the $p_{\pi}(O_t) \rightarrow d_{\pi^*}(W)$ transitions is centred at 49100 cm^{-1} and 49300 cm^{-1} for ligand and complex respectively [12]. This is in agreement with the co-ordination of the Mn (II) ions in the lacunary region of the ligand and not to the terminal oxygen atoms. The broader band centred at 39732 cm^{-1} in the ligand spectrum belongs to the $p_{\pi}(O_{c,e}) \rightarrow d_{\pi^*}(W)$ change transfer transition in the tricentric bonds. This band is shifted towards lower energies in the case of the complex (at 39467 cm^{-1}).

Information about the local environment of Mn (II) ions have been obtained by means of d-d transitions from the visible electronic spectrum performed in aqueous solution.

Electronic spectrum of the manganese(II)-complex obtained in the visible range contains one absorption band up to 30000 cm^{-1} (Fig. 4) for the $Mn^{II} \rightarrow O$ charge transfer transition. The Gaussian deconvolution of the spectrum shows the presence of a band centered at 29340 cm^{-1}. Taking into account the geometry of the complex similar to that of other sandwich-type HPOM with four 3d transition ions [5-7], this band was assigned to the $^6A_{1g}(S) \rightarrow {}^4E_g(D)$ transition of the Mn^{II} ions in O_h distorted symmetry [12].

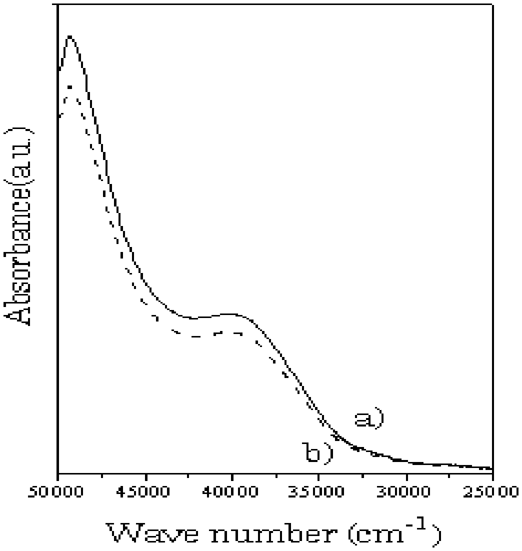

Fig. 3. The UV spectra of the ligand (a) and complex (b).

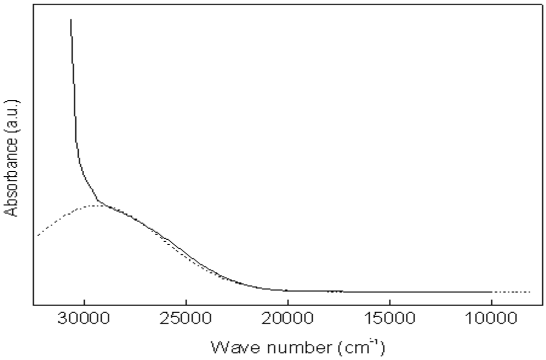

Fig. 4. Visible spectrum of the Mn^{II}–HPOM complex (the solid line) and the Gaussian component obtained by deconvolution (the pointed line).

3.3. EPR spectra.

Powder EPR spectra of the complex obtained at room and 80 K (Fig. 5 and 6) temperatures were interpreted by considering antiferromagnetic couplings between the Mn^{II} ions of the centrosymmetric rhomb-like Mn_4O_{16} cluster using a spin Hamiltonian which contains the Zeeman and zero field splitting terms [13]:

$$H = \mu_B BgS + D\left[S_z^2 - S(S+1)/3\right] + E\left(S_x^2 - S_y^2\right)$$

Taking into account the presence of the signals at ≈ 655 G, 1045 G, 1650 G and 3460 G, the spectrum obtained at room temperature was simulated with the following parameters: the S = 5 spin state, the isotropic value g = 2.0 and the axial D = 0.030 cm^{-1} and rhombic E = 0.006 cm^{-1} zero-field splitting parameters.

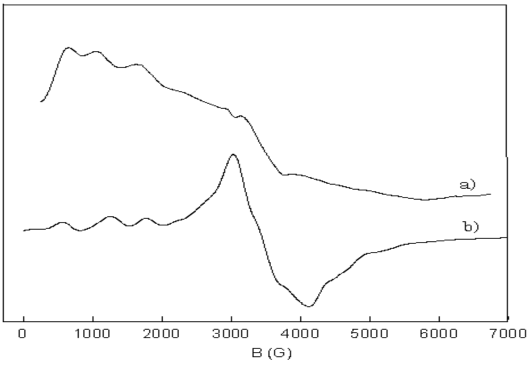

Fig. 5. Powder EPR spectra of the complex obtained in the X band at (a) T = 293 K (9.617 GHz) and (b) the simulated spectrum. In the inset are represented the exchange pathways for the tetranuclear manganese cluster.

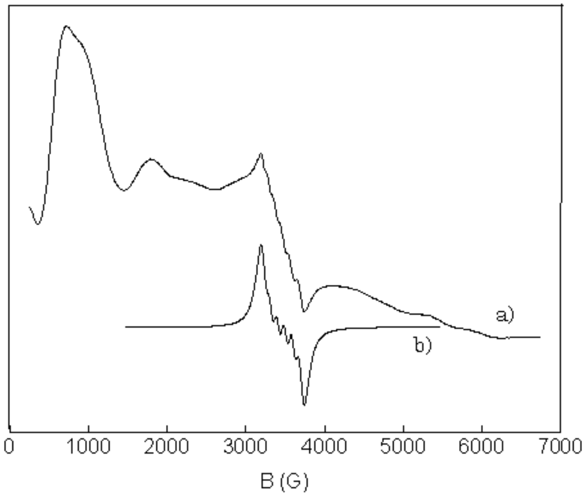

Fig. 6. (a) Powder EPR spectrum of the complex obtained at T = 80 K and (b) the simulated hyperfine structure of the signal at 3460 G.

The hyperfine structure of six lines observed on the signal at ≈ 3460 G is due to the interaction between the unpaired electrons with the ^{55}Mn (I = 5/2) nucleus [13]. The obtained value for the hyperfine constant, A = 94 G, is typical for a single Mn^{II} ion and suggests the tendency of localization of the unpaired electrons on the parent ions with the decrease of the temperature [14].

4. Magnetic susceptibility measurements.

The magnetic susceptibility data were corrected by the diamagnetic contribution by means of Pascal constants. In the temperature 77 – 290 K the molar magnetic susceptibility follows a Curie – Weiss behavior (Fig. 7). The obtained effective magnetic moment is μ_{eff} = 11.81 μ_B and the value of Curie is $\theta = - 5.4$ K.

The magnetic moment value and the negative θ correspond to a system with S = 5 ground state, obtained through antiferromagnetic exchange between the manganese (II) spins.

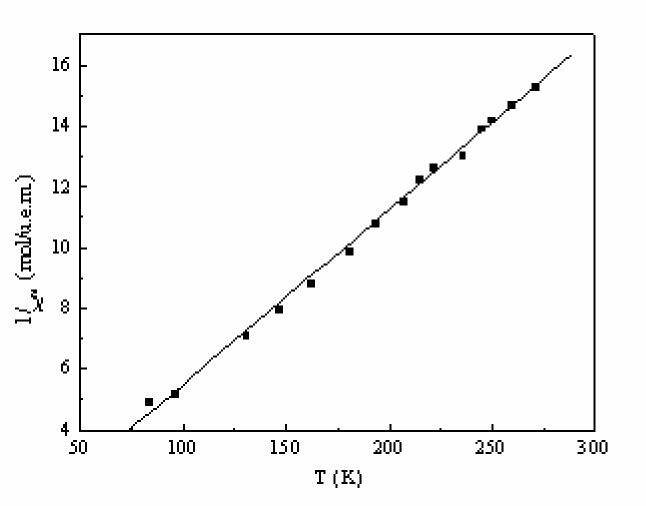

Fig. 7. The temperature dependence of the magnetic susceptibility for the $Na_{10}[Mn_4(H_2O)_2(AsW_9O_{34})_2]\cdot 27H_2O$ complex.

4. Conclusions

The sandwich-type complex $Na_{10}[Mn_4(H_2O)_2(AsW_9O_{34})_2]\cdot 27H_2O$ containing a centrosymmetric rhomb-like Mn_4O_{16} cluster was investigated by means of spectroscopic methods (FT-IR, Vis, EPR).

The shift of the $\nu_{as}(W–O_e–W)$ and $\nu_{as}(W–O_c–W)$ vibration bands for the bonds from edge and corner-sharing octahedra respectively in the complex FT-IR spectrum compared to the ligand spectrum indicated the coordination of the Mn^{II} ions in the lacunary region of the AsW_9O_{34} fragments.

The local symmetry around the metallic centers is octahedral distorted as arrised from the Vis spectrum of the complex.

EPR spectrum obtained at room temperature was interpreted by considering the spin state $S = 5$ and the parameters: $g = 2.0$, $D = 0.030\ cm^{-1}$ and $E = 0.006\ cm^{-1}$, in terms of an antiferromagnetic coupling between the Mn^{II} ions.

REFERENCES

1. A. Müller, F. Peters, M.T. Pope, D. Gatteschi, Chem. Rev. 98 (1998) 238.
2. X. Zhang, T.M. Anderson, Q. Chen, C.L. Hill, Inorg. Chem. 40 (2001) 418.
3. D.L. Barnard, C.L. Hill, T. Gage, J.E. Matheson, J.H. Huffman, R.W. Sidwell, M.I. Otto, R.F. Schinazi, Antiviral Res. 34 (1997) 27.
4. M. Fournier, C. Feumi-Janton, C. Rabia, G. Hervé, S. Launay, J. Mater. Chem. 2 (1992) 971.

5. C.J. Gómez-Garcia, E. Coronado, J.J. Borrás-Almenar, Inorg. Chem. 31(9) (1992) 1665.
6. U. Kortz, Y.P. Jeannin, A. Tézé, G. Hervé, S. Isber, Inorg. Chem. 38 (1999) 3670. A. Müller, C. Beugholt, P. Kögerler, H. Bögge, S. Bud'ko, M. Luban, Inorg. Chem. 39 (2000) 5176.
7. L.-H. Bi, R.-D. Huang, J. Peng, E.-B. Wang, Y.-H. Wang, C.-W. Hu, J. Chem. Soc. Dalton Trans. 121 (2001).
8. R. Contant, M. Abbesi, J. Canny, Inorg. Chem. 36 (1997) 961.
9. W.H. Knoth, P.J. Domaille, R.I. Harlow, Inorg. Chem. 25 (1986) 1577.
10. R. Massart, R. Contant, J.M. Fruchart, J.F. Ciabrini, M. Fournier, Inorg. Chem. 16 (1977) 2916.
11. B.P. Lever, Inorganic Electronic Spectroscopy, Elsevier, New York, 1984. A. Bencini, D. Gatteschi, Transition Metal Chemistry, vol.8, Marcel Dekker, New York, 1982, p.78.
12. O. Cozar, L. David, V. Chiş, O. Cosma, V. Znamirovschi, G. Damian, Appl. Magn. Reson. 8, 235 (1995).

STUDIA UNIVERSITATIS BABEŞ-BOLYAI, PHYSICA, LI, 2, 2006

USING STABLE ISOTOPES TO IDENTIFY GEOGRAPHICAL ORIGIN OF WINES

STELA CUNA[1], C. CUNA[1], GABRIELA BALAS[1], O. COZAR[2]

ABSTRACT. The content of ^{18}O in water from wine is determined by IRMS and is used for the detection of addition of water, for the characterisation of the geographical origin of wines and for the authentication of the year of vintage. The European Community has adopted the determination of ^{18}O from wine as an official method for the analysis of wines and has included this parameter in the E.U.Wine Databank. This paper presents some results concerning the use of $^{18}O/^{16}O$ isotopic ratio of the water of wine to identify the geographical origin of wines.

Introduction

The natural ratio of stable isotopes in plant organic materials is not constant, but depends on the original isotopic content of the molecules used by the plant for photosynthesis, water and carbon dioxide and on isotopic fractionation during biosynthetic pathways. Both precursor molecules are characterized by specific isotope ratios of the hydrogen, carbon, and oxygen. The isotope ratios of hydrogen ($^{2}H/^{1}H$), carbon ($^{13}C/^{12}C$) and oxygen ($^{18}O/^{16}O$) can be measured very accurately by Isotope Ratio Mass Spectrometry (IRMS).

The amount of the heavy isotopes in water and carbon dioxide and even their distribution in the sugar and enthanol molecule are significantly influenced by geo-climatic conditions of the provenance region, the type of plant, the mechanism of photosynthesis, and the year of harvest [1].

The $^{18}O/^{16}O$ isotope ratio of the wine water and the $(D/H)_{II}$ (fraction II of distillate wine sample) ratio of the wine ethanol are parameters that may be used for the control of the geographical provenance, the period of vintage or the detection of a water dilution of wine or grap must [2]. The applicability of the isotopic content is based on the fact that precipitation and groundwater show a special pattern in dependence of the geographical origin. The isotopic signature of water usually is changed by phase transitions within the atmospheric water cycle. The resulting spatial and temporal differences in $\delta^{18}O$ and $\delta^{2}H$ values in water depend on amount of precipitation, temperatures (annual and seasonal effects), distance from sea (continental effect) and

---

[1] National Institute for Research and Development of Isotopic and Molecular Technologies, Donath Str. 71-103, Cluj Napoca 400293, Romania

[2] Babes-Bolyai University, Faculty of Physics, Kogalniceanu Str. 1, Cluj-Napoca

altitude. The $\delta^{18}O$ and $\delta^{2}H$ values of water show a linear correlation. Corresponding to the isotope fractionation of deuterium and ^{13}C in ethanol during a fractionated distillation, plants discriminate against the lightest isotopic species of water during transpiration. Hence the water of plant tissues is enriched in ^{18}O and ^{2}H content. The correlation of the $\delta^{2}H$ versus $\delta^{18}O$ value of the water can be changed due to a relative stronger enrichment factor of oxygen in comparison to hydrogen.

Because the extent of the transpiration and in consequence, the degree of enrichment of the heavy isotopes is influenced by the local climate, the ^{18}O and ^{2}H content in grape water compared to surface and groundwater can be used to prove an addition of water to a wine.

Method

The $^{18}O/^{16}O$ isotopic ratio of the water of a grape must or wine is determined by IRMS using the ions m/z 46 ($^{12}C^{16}O^{18}O$) and m/z 44 ($^{12}C^{16}O_2$) which are obtained after equilibrium of the isotopic exchange of water and carbon dioxide. The exchange reaction is

$$^{12}C^{16}O_2 + H_2O \Leftrightarrow {}^{12}C^{16}O^{18}O + H_2{}^{16}O \qquad (1)$$

This reaction proceeds via the solvent hydrogen carbonate and is temperature dependant. The carbon dioxide in the vapour phase is used for analysis. For equilibration the sample flasks are filled with 5 ml sample and carbon dioxide is introduced. Then the batch of the sample bottles is placed in a thermostatically controlled water bath at 25^0C. The equilibrium duration is about 24 hours. After equilibration the carbon dioxide of the sample bottles is transferred to the mass spectrometer through a cryogenic trap maintained at -70^0C (liquid nitrogen and alcohol mix) to remove water vapour and ethanol. The measurements are performed versus calibrated laboratory standard water. The relative difference of the ion intensity ratio of m/z 46 and 44 (I46/I44) between the samples and standards are measured in ‰ and are expressed in the relative difference $\delta^{18}O$ ‰ versus the Vienna Standard Mean Ocean Water (SMOW). The method was adapted by the EC-Regulation 822/97 [3], [4]. For the determination of the $\delta^{18}O$ and $\delta^{13}C$ values, an IRMS, type ATLAS designed by Varian, Bremen, was used with a precision of $\pm$ 0.3‰.

Results and Discussion

The isotopic composition of ^{13}C, ^{18}O from 14 wine samples is presented in Table1.

Table 1.

The isotopic composition of the ^{13}C, ^{18}O from 14 wine samples

Sample	Type of wine	$\delta^{18}O_{SMOW}$ (‰)	$\delta^{13}C_{PDB}$ (‰)
1.	Cabernet Sauvignon, Tg. Bujor, 2004, red wine	0.10	-26.74
2.	Cabernet Sauvignon, Murfatlar, 2004, red wine	0.23	-28.41
3.	Cabernet Sauvignon, Tohani, 2003, red wine	5.35	-24.67
4.	Cabernet Sauvignon, V. Calugareasca, 2004, red wine	-0.18	-27.48
5.	Cabernet Sauvignon, V. Calugareasca, 2003, red wine	4.16	-24.86
6.	Cabernet Sauvignon, Tohani, 2004, red wine	1.89	-27.05
7.	Cabernet Sauvignon, Murfatlar, 2003, red wine	1.13	-26.98
8.	Cabernet Sauvignon, Bujoru, 2003, red wine	3.40	-24.57
9.	Feteasca Regala, Copou, 2002, white wine	-5.87	-29.00
10.	Feteasca Regala, Aiud, 2002, white wine, FINAL	-1.60	-25.56
11.	Feteasca Regala, Dragasani, 2002, white wine, START	-3.46	-28.18
12.	Feteasca Regala, Copou, 2004, white wine	-0.52	-26.22
13.	Feteasca Regala, Aiud, 2004, white wine	-1.15	-25.93
14.	Feteasca Regala, Dragasani, 2004, white wine	0.80	-27.89

It is necessary to determine both $\delta^{18}O$ and $\delta^{13}C$ for a complete characterisation of a wine [5], [6], [7].

Isotopic content of ^{18}O varies between -5.87 ‰ and 5.35 ‰ and depends on the geographical origin of wines and the precipitations on the harvest area. There is a difference in $\delta^{18}O$ values of the county Murfatlar wines (0.23-1.13‰) and the county Bujoru wines (0.10-3.40‰). For the same region and the same type of wine, there are differences between years of harvest. Meteorological conditions and precipitations are changing from year to year and they are responsible for these differences. Thus, we can observe a difference from 5.35 ‰ to 1.89 ‰ for Cabernet Sauvignon from Tohani region in 2003 and 2004, respectively.

Isotopic composition of ^{13}C varies between -24.57‰ and -29‰. These values are typical for plants with C3 metabolism. CO_2 assimilation process by photosynthesis is influenced by temperature and precipitations quantities, thus some variations are due to this stress factors for plants. In this way one can explain the difference between $\delta^{18}O$ value for Feteasca Regala, Copou region, harvest 2004 (-26.22‰) and the value for the same wine, but harvest 2002 (-29‰).

Conclusions

The $^{18}O/^{16}O$ isotopic ratio of the water of wine was determined by IRMS using CO_2, which was obtained after equilibration of wine and carbon dioxide. The samples of wine from the 2002, 2003 and 2004 vintages and from different vineyard of Romania were analyzed. We developed this method in order to set up in the future the databank of isotope ratios of authentic samples of wine as well as for the routine control of Romanian wines being on market .

REFERENCES

1. N. Christoph, A. Rossmann, S. Voerkelius, *Possibilities and Limitations of Wine Authetication Using Stable Isotope and meteorological Data, Data Banks and Statistical Tests*, Mitteilungen Losterneuburg 53, pp. 23-40 (2003)
2. G. Versini, A. Monetti, F. Reniero, *Monitoring authenticity and regional origin of wines by natural stable isotope ratios analysis*. In Wine-Nutritional and Therapeutic Benefits; Watkins, T.R., Ed.; ACS Symposium Series 661; American Chemical Society: Washington, DC, pp113-130 (1997)
3. EU, 1997, EC-Regulation 822/1997 amending E.C. Regulation No. 2670/90: *Determination of the isotopic ratio* $^{18}O/^{16}O$ *of the water content in wines*, Off.J.Eur.Communities L117, pp 10-12
4. B. Hobbach, H. Forstel, H. Ottender and H. Hutzen, *The stable isotope ratio of* ^{18}O *and* ^{16}O *as a means to evaluate foreign wine*, Z. Lebensm. Unters.Forsch. 198, pp.223-229 (1994)
5. G.J. Martin, B.L. Zang, N. Naulet, N and M.L. Martin, *Deuterium transfer in the bioconversion of glucose to ethanol studied by specific isotope labelling at the natural abundance level*, J.Am.Chem.Soc.108, pp 5116-5122 (1986)
6. C. Bauer-Christoph, H. Wachter, N. Christoph, A. Rossmann and L. Adam, *Assignment of raw material and authentication of spirit by gas chromatography, hydrogen – and carbon-isotope ratio measurements*, Z.Lebensm.-Unters. Forsch.A 204(6), pp 445-452 (1997)

STUDIA UNIVERSITATIS BABEŞ-BOLYAI, PHYSICA, LI, 2, 2006

THE INFLUENCE OF DEPOSITION PARAMETERS ON STRUCTURAL AND ELECTRICAL RESISTANCE OF EPITAXIAL BI:2212 THIN FILMS

S.MANOLACHE[*] AND A.V.POP[*]

ABSTRACT. The deposition parameters (sputtering pressure, substrate temperature, d.c.plasma power and sputtering gas composition) for the deposition of thin Bi:2212 films by d.c.magnetron sputtering have been modified.

X-ray diffraction and electrical resistance function of temperature, shows the influence of temperature substrate on the intergrowth defects.

Keywords: Bi:2212 thin film, DC magnetron sputtering, growth conditions, XRD, resistivity.

1. Introduction

The engineering of thin-film structures has been found useful in a wide range of applications during the past years. In order to understand the mechanism of high Tc superconductors (HTS) and to investigate the principles of device operation, it is important to obtain single crystal and thin films of high quality.

Moreover, HTS's are well known as very sensitive materials to external factors: small changes in the growth conditions can lead to significantly different quality. A new approach to the growth of HTS thin films is necessary and new methods to wisely control growth are of key importance for the development of the field. In general, for device fabrication or integration, component thin films should fulfill several requirements[1].

(a) A certain substrate–film relationship is necessary (e.g. lattice matching, wetting and chemical stability and compatibility).

(b) A certain morphology/roughness is necessary (optimum growth conditions should be found and knowledge of the growth mechanism is useful in this respect).

(c) Relatively large clean surfaces are desired; i.e. without impurity precipitates–segregates.

(d) Controlled properties, usually uniform and reproducible,

High quality HTS thin films fabrication and multilayer are indispensable for the fabrication of integrated junction circuits. The films with c-axis aligned to the film plane appear to be preferably suited for the fabrication of sandwich type SNS and SIS Josephson and quasiparticle tunnel junctions [2]. Bi:2201

---

[*] Faculty of Physics, University Babes-Bolyai, Cluj-Napoca ,Romania

thin films have been much attention from the viewpoint of their utilization such as artificial intrinsic Josephson junction, a buffer layer for fabrications of Bi:2212 and Bi:2223 thin films [3].For the deposition of BSCCO films difficulties arises from possible phase mixture and oxygen over doping. Thin films of Bi:2212 grow epitaxially depending on the substrate material, thermodynamic and kinetic growth conditions. The epitaxial growth of thin films of Bi:2212 has been realized on substrates like SrTiO3, LaAlO3 and MgO [4-7]. Usually these films were grown with their c-axis perpendicular to the substrate surface, since c-axis growth is thermodynamically favored growth direction. Sputtering is one of the most common vacuum techniques currently applied for superconducting oxide thin film growth. The sputter deposition technique can tolerate quite high gas pressure while still giving controllable growth rates, as long as the targets surface is insensitive to oxidation.

Here we present the optimization of temperature substrate and concentration of oxygen in sputtering gas for fabrication of epitaxial Bi:2212 films. The thin films were characterized by X-ray diffraction and electrical resistivity measurements versus temperature.

2. Experimental

Bi:2212 thin films were deposited onto (100) $SrTiO_3$ heated single crystal substrate by using DC magnetron sputtering system.

In the sputtering chamber, the material is removed from the polycrystalline target (cathode) by the ion bombardment. The system uses an on-axis geometry: the substrate and planar target is positioned faces each other at a distance of 10-20 mm. The film substrate is mounted on a heater, placed at some distance outside the ring magnet. In the DC mode, the plasma is formed around the ring target positioned above the magnetron (the ring magnet) which enhances the sputtering rate. In order to control the atmosphere during the deposition process, the sputtering chamber is connected to a turbo-molecular pumped vacuum system and the sputtering gases (Ar and oxygen) are vented from the top of the gun to the vicinity of target. The partial pressure of each gas is adjusted by a needle valve. The film thickness is measured by the quartz sensor mounted near the substrate.

A major problem that appears during the deposition of Bi:2212 thin films are the Bi losses. The film composition function of temperature shows that the Bi ratio gradually diminishes for temperature above 600 ^{0}C [8]. In order to compensate for this loss, a bismuth enriched target has been synthesized with chemical composition $Bi_{2.6} Sr_{1.97} Ca_{0.97} Cu_{2.4} O_y$.

For the synthesis of target the solid state reaction route was used. The resulting material is superconducting with Tc=82K. XRD shows that Bi:2212 is the majority phase by some traces of Bi:2201 and CuO. The effect of the sputtering pressure on the epitaxy of Bi:2212 film has been investigated by the deposition of many thin films under various total pressures ranging from 0.5 to 1.2 mbar .Above 1mbar the plasma become increasingly unstable .In order to prevent target damage the depositions were carried out at a total pressure of 0.9 mbar. The in-situ thin films were obtained by on-axis d.c.magnetron sputtering. The optimal parameters used for fabrication of epitaxial quality Bi:2212 thin films were: sputtering gas pressure of 0.9 mbar (with a ratio 1/1 between the argon and oxygen partial pressures), the substrate temperature 840 ^{0}C and d.c. plasma power between 20W and 30W. The increase of Tc for Bi:2212 thin films arise by optimizing the oxygenation of BiO bilayers [9]. The oxygen content of our thin films was adjusted by an oxygenation treatment after the high temperature annealing. The oxygen pressure was of 0.15 mbar, the temperature of thin film 500 ^{0}C and the oxygenation time of 40 minute. The substrate temperature is one of the most important parameter for obtained high quality films, because of the influence on the stability of Bi:2212 phase and on the Bi losses.

For the sputtering time $t_{sp.}$=60 minutes, and substrate temperatures T_s = 840^{0}C, 850^{0}C and 860^{0}C, 865 the thin films named F_1, F_2, F_3 and F were obtained.

The X-ray powder diffraction pattern was taken for some of examined samples using XD8 Advance Bruker diffractometer using CuK_α radiation (λ=1,541874 Å).

The resistance of the samples was measured using four-probe method in the temperature range between 4.2K and 300K using a Keithley 2182 nanovoltmeter.

3. Results and discussions

Figure 1 shows the X-ray diffraction pattern obtained for the F1 thin film of Bi:2212 deposited by using for substrate the temperature T_s = 840^{0}C. The peak indexation indicates that only (00l) reflexions are observed for thin films .

This behavior suggests that the film is highly oriented. No additional peak can be distinguished from the background , indication that the film is free from bulk secondary phases. Bi:2212.Similar behavior was evidenced for F2 film deposited at T_s = 850^{0}C. By increasing substrate temperature to T_s = 860^{0}C, small amount of Bi:2223 phase was evidenced.

Fig.2 shows the effect of substrate temperature on the (002) line of $\theta - 2\theta$X ray diffraction pattern of thin films deposited on $SrTiO_3$ substrate. A thin and symmetric (002) peak of Bi:2212 phase is measured for the optimal temperature of T_s=840 ^{0}C .At higher temperatures than 840 ^{0}C ,the Bi:2223 phase intergrowth is favored and the epitaxial quality is reduced [10].

The intergrowth is the dominant stacking fault in the BSCCO system. In the intergrowth, layers of Bi:2201, Bi:2212 and Bi:2223 appear in the overall structure. In our films by the chemical composition corresponding to the

Bi:2212 phase, inserted 2223 layers may appear in the 2212 matrix without causing any compositional change.

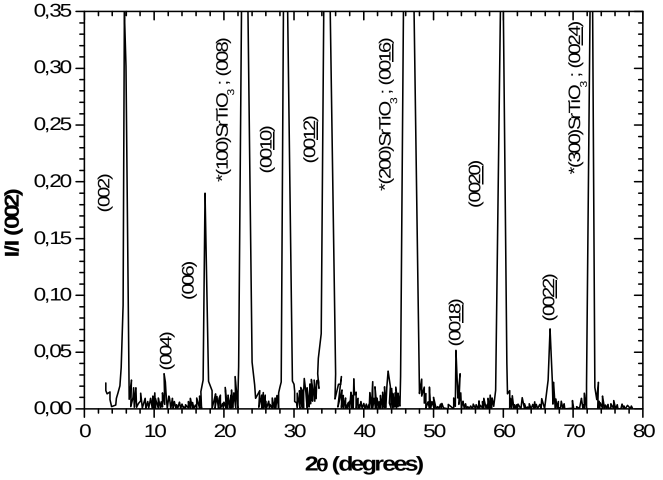

Fig.1. X-ray diffraction pattern of Bi:2212 film deposited on $SrTiO_3$ substrate. The substrate (i00) reflexions are labeled by asterisk.

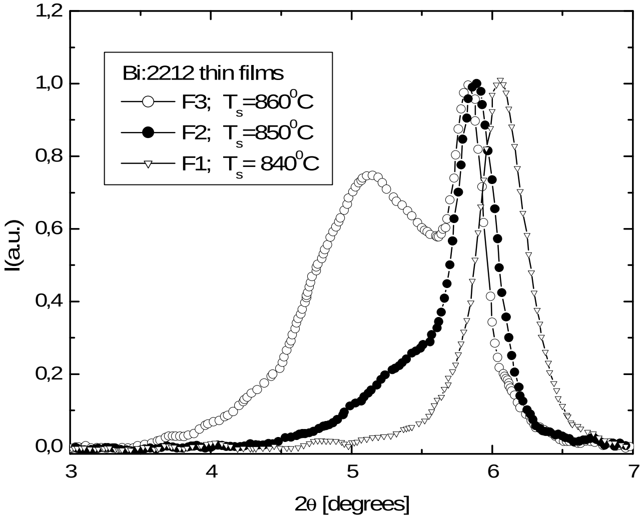

Fig.2. The variation of the normalized (002) peak obtained by X-ray diffraction on Bi:2212 samples deposited on $SrTiO_3$ at different temperatures

By increasing substrate temperature, the angle 2 θ corresponding to position of (002) maximum decrease, suggesting that the intergrowth of Bi :2223 increase. For low densities of intergrowth are difficult to detect by X-ray diffraction but have a prominent effect on the electrical resistance. .

Figure 3 shows that our samples are characterized in normal state by a linear temperature dependence of the electrical resistivity:

$$\rho = \rho_0 + \alpha * T \qquad [1]$$

where ρ_0 is the residual resistivity and α is the slope of resistivity in the normal state. As shown in Table1, the ρ_0 and α values decrease with increasing substrate temperature.

The sample F3 with T_c = 86K shows a residual resistivity ρ(T=300K) =900 μΩcm. These values characterize the pure Bi:2212 superconducting system [4,11]. The kink around 110K (arrow in fig.3) indicates the presence of a small quantity of Bi:2223 intergrowth in the film by substrate temperature of 850 ^{0}C. This result agrees with the shift of (002) line from optimal position to links (around $2\theta = 5$degrees) in fig.2. For these samples containing a few intergrowth of Bi:2223 , XRD peaks are only slightly displaced away from the pure Bi:2212 pattern. The sample showing a kink at 110K showed a vanishing extrapolated zero temperature resistivity ρ(T=0K), and a critical transition temperature T_c =80.5K.

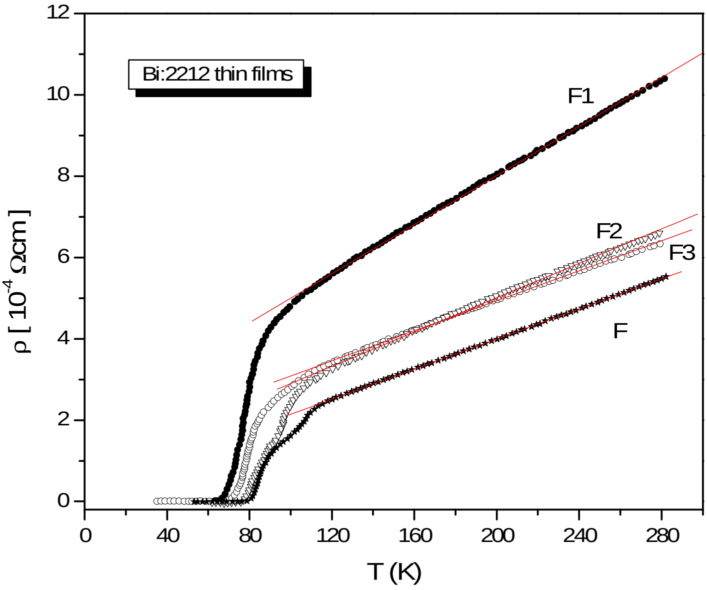

Fig.4. The resistivity versus temperature for thin films with different substrate temperatures . The kink around 110K indicated by arrow indicates the intergrowth of Bi:2223 phase.

Table 1.
The influence of substrate temperature on electrical resistivity parameters obtained for Bi:2212 films.

Thin Films	Substrate temperature T_S [^{0}C]	Residual resistivity ρ_0 [μΩ cm]	dρ/dT [μΩ cm K^{-1}]	T_c [K]
F_1	840	1980	3.01	78.8
F_2	850	1212	2.09	79.5
F_3	860	900	1.85	84.5
F	840	280	1.8	84.5

The changes of ρ_0 and the slope of resistivity agree with the change in the Bi:2223 intergrowth.

Another parameters sensitive to substrate temperature are the midpoint critical transition temperature (T_c), the transition width and the temperature for zero resistivity ($T_c(\rho=0)$). Figure 3 show the temperature dependence of electrical resistance for our Bi:2212 thin films in the region of transition from normal to superconductor. Samples F1 and F2 shows a single step transition, sample F3 shows a kink around 100K and sample F3 a two step transition.

The midpoint critical transition temperature for Bi:2212 increases by increasing substrate temperature (table 1)

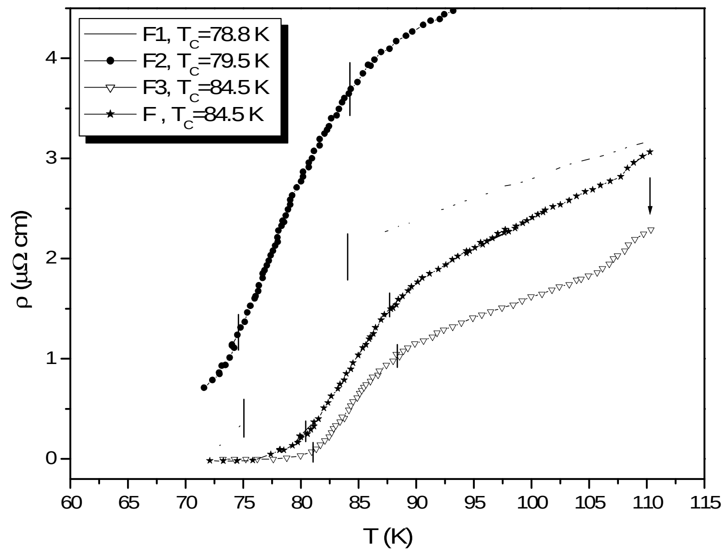

Fig.3. The temperature dependence of electrical resistance for our Bi:2212 thin films in transition region.

4. Conclusions

The change of substrate temperature for the deposition of Bi:2212 films by d.c. magnetron sputtering, lead to changes in structural and electric properties .

XRD shows that the synthesized films for substrate temperature T_s = 840 K was single Bi:2212 phase ,epitaxial and oriented with c-axis perpendicular to substrate surface.

By increasing T_s up to 860^0C lead to a few intergrowth of Bi:2223 (with T_c =110K).Electrical resistivity shows in normal state a metallic behavior.

Residual resistivity, the slope of ρ(T) and the midpoint transition temperature of Bi:2212 were influenced by substrate temperature.

Superconducting transition shows a single or in two step.

The presence of intergrowth is related by the kink or a step around 110 K in the resistivity curve versus temperature and by the decrease of residual resistivity.

REFERENCES

1. K Endo, P Badica, H Sato and H Akoh, *Supercond. Sci. Technol*. **19**, (2006) S221–S225;
2. J.Geerk, X.X.Xi, G.Linker, *Z.Phys.B***73**, (1988) 1327;
3. T.Satoh, J.Fujita, T.Yoshitake, H.Igarashi, S.Miura,N.Matsukura,H.Tsuge, *Physica C* **185-189**, (1991) 2059;
4. P.Wagner,F.Hillmeyer,U.Frey,H.Adrian, T.Steinborn, L.Ranno,A.Elschner, I.Heyvaert, Y.Bruynserade, *Physica C* **215**, (1993) 123;
5. L.X.You, A.Yurgens,D.Winkler, C.T.Liu, B.Liang, *Supercond.Sci.Technol.***19**, (2006) S205;
6. A.V.Pop,G.Ilonca, M.Pop, *JOAM* **8**, (2006) 480 ;
7. R.Rossler, J.D.Pedarnig, Ch.Joos, *Physica C* **361**, (2001) 13-21;
8. T.Onishi, N.Fujiwara,S.Kishida, *Physica C* **426-431**, (2005) 1439;
9. J.M.Grace, D.B.McDonald, M.T.Reiten, J.Olsen,R.T.Kampwirth, K.E.Gray, *J.Appl.Phys.***70**, (1991) 3867;
10. T.Watanabe, T.Fuji,A.Matsuda, *Phys.Rev.Lett.***79**, (1997) 2113;
11. L.Ranno,D.Marquez-Garcia,J.Perriere, P.Barboux, *Phys.Rev.B* **48**, (1993) 13945;
12. S.Labdy,S.Megtert,H.Raffy, *Sol.State Commun*.**85**, (1993) 491.

STUDIA UNIVERSITATIS BABEŞ-BOLYAI, PHYSICA, LI, 2, 2006

RAMAN SPECTROSCOPY OF LEAD-PHOSPHATE GLASSES WITH IRON IONS

D. A. MAGDAS*, O. COZAR, I. ARDELEAN, N. VEDEANU

ABSTRACT. The structure of $xFe_2O_3{\cdot}(100\text{-}x)[2P_2O_5{\cdot}PbO]$ glass system with $0 \leq x \leq 10$ mol% was investigated by Raman spectroscopy. The characteristic bands of these glasses due to the stretching and bending vibrations were identified and analyzed by the increasing of Fe_2O_3 content. This fact allowed us to identify the specific structural units which appear in these glasses and to deduce the role of the Fe_2O_3 oxide on the structural changes of $2P_2O_5{\cdot}PbO$ network. At high Fe_2O_3 content a depolymerization of the phosphate network appears and the short phosphate chain units or ring structures are formed, too.

Introduction

Phosphate glasses are of technological interest due to their several unique properties, such as high thermal expansion coefficient, low viscosity resulting in low melting and softening temperatures, UV transmission and other optical properties, and electrical conduction. The technological importance of these glasses requires a detailed understanding of the molecular and structural chemistry in order for glasses to be designed for particular applications [1].

The practical applications of phosphate glasses are limited by their poor chemical durability. The physical and chemical properties of phosphate glasses can be optimized by controlling the melting conditions and chemical composition [2]. The chemical durability of lead-phosphate glasses increases dramatically with the addition of Fe_2O_3 and PbO [3].

In this work the glass system $xFe_2O_3{\cdot}(100\text{-}x)[2P_2O_5{\cdot}PbO]$ with $0 \leq x \leq 10$ mol% are characterized by Raman spectroscopy, in order to understand the role of iron oxide on the local structure.

Experimental

The starting materials used in the present investigation were $(NH_4)_2HPO_4$, PbO, and Fe_2O_3 of reagent grade purity. The samples were prepared by weighing suitable proportions of the components, powder mixing and mixture melting in sintered corundum crucibles at 1250^0 C for 5 min. The mixtures were put into the furnace directly at this temperature. The obtained glass-samples were quenched by pouring the molten glass on a steel plate.

---

* Faculty of Physics, Babes-Bolyai University, 400084 Cluj-Napoca, Romania
amagdas@phys.ubbcluj.ro

The FT-Raman spectra were recorded with a Bruker FRA 106/S Raman accessory attached to the Bruker Equinox 55 FT-IR spectrometer equipped with an InGaAs detector working at room temperature. The FT-Raman spectra were recorded in backscattering geometry with a resolution of 4 cm^{-1}.

Results and Discussion

The Raman spectra of $x\cdot Fe_2O_3(1-x)[2P_2O_5\cdot PbO]$ glass system with $0\leq x\leq 10$ mol% are show in Fig. 1. It can be observed that their shapes are changed with the increase of Fe_2O_3 content. For x=0mol% the Raman spectrum shows the characteristic bands of $2P_2O_5\cdot PbO$ matrix. It is know that PbO oxide acts as modifier or network former in glass matrix [4-7]. The presence in the Raman spectra of the broad band at about 323 cm^{-1} may be attributed to the presence of Pb-O bonds in these glasses [8]. The 693 cm^{-1} band is attributed to the P-O-P symmetric stretching vibrations of the Q^2 tetrahedrons [1, 9, 10], while the weak shoulder from 1076 cm^{-1} is due to symmetric stretching vibration (PO_3) in Q^1 groups [11]. In the Q^n terminology, n represents the number of bridging oxygens (BO) per PO_4 tetrahedron. The bands from 1160 cm^{-1} and 1255 cm^{-1} have been attributed to symmetric and asymmetric stretching motions of the two non-bridging oxygen (NBO) atoms bonded to phosphorous atoms (PO_2) in the Q^2 phosphate tetrahedron [8, 9, 12].

With the increases of modifier oxides content, the band from 693 cm^{-1} shifts to higher wavenumber (699 cm^{-1}) and also decreases gradually in intensity. For highest concentration of modifier oxides (x= 10 mol%) this band almost disappears.This band is assigned to the P-O-P symmetric stretching vibration of the long-chain phosphate glasses. When the chain length decreases [13] the frequency of this band increases to 699 cm^{-1}. The shift in the frequency of the band is attributed to a change in the in-chain P-O-P bond angle depending on the effect of the network modifier on phosphate glass structure [14, 15]. The larger wavenumber of the band is a result of the smaller P-O-P bond angle, characteristic for shorter phosphate chain length [1].

With the addition of modifier oxides the bands from 1076, 1160 and 1255 cm^{-1} decreases gradually in intensity. For highest concentration of modifier oxides (x= 10 mol%) these bands almost disappear. This fact could be explained trough the gradual depolymerization of the long phosphate chain with the increases of the modifier oxides content.

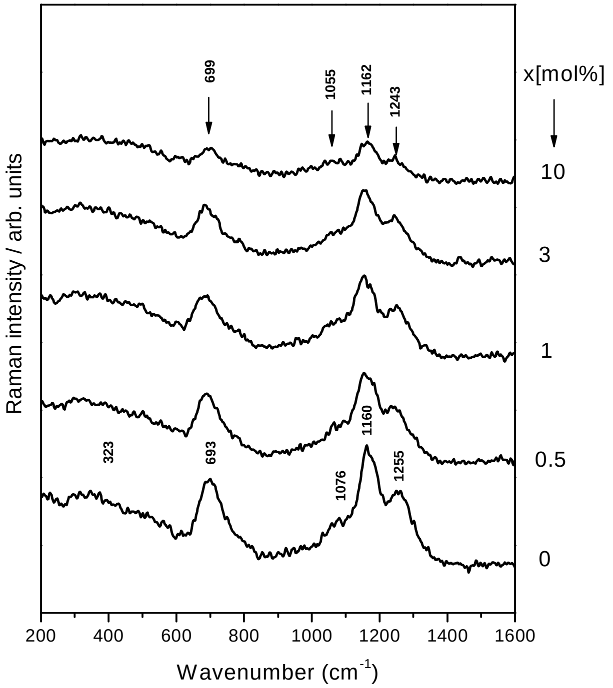

Fig. 1. Raman spectra of $xFe_2O_3 \cdot (100-x)[2P_2O_5 \cdot PbO]$

The change in the wavenumber and width of the bands depending on the kind and concentration of network modifiers in phosphate glasses has also been investigated and reported by others authors [14, 15]. Rouse et al. [14] have pointed out that the decrease of the O-P-O stretching frequency is essentially due to an increase of the O-P-O angle and to larger metal-oxigen force constant [10].

Conclusions

The shape of the Raman spectra is influenced by the presence of iron oxide in the studied glasses. With the increasing of Fe_2O_3 content, the bands characteristic to phosphate glasses decreasing strongly in intensity. The 693 cm^{-1} band assigned to the P-O-P symmetric stretching vibration is shifted to 699 cm^{-1} due to the decrease of the chain length with the increase of iron oxide content.

From these considerations we concluded that with the addition of Fe_2O_3 in the glass systems a very strong depolimerization appears.

REFERENCES

1. J. Koo, B. Bae and H. K. Na, J. Non-Crystal. Solids, 212, 173 (1997)
2. S. T. Reis, M. Karabulut, D. E. Day, J. Non-Cryst. Solids, 292, 150 (2001)
3. R. K. Brow, C. M. Arens, X. Yu, D. E. Day, Phys. Chem. Glasses, 35, 132 (1994)
4. U. Selvaraj and K. J. Rao, J. Non-Crystal. Solids, 104,300 (1988)

A. J. Bourdillon, F. Khumalo and J. Bordas, Philos. Mag. B37, 731, (1978)

5. S. R. Elliott, “Physics of Amorphous Materials”, (2nd Edn, Longman, New York, 1990)
6. K. J. Rao, B. G. and S. R. Elliott, J. Mater. Sci., 20,1678, (1985)
7. D. A. Magdas, O. Cozar, I. Ardelean, L. David, Int. J. Mod. Phys. B19, 1815 (2005)
8. O. Cozar, D. A. Magdas, L. Nasdala, I. Ardelean, G. Damian, J. Non-Cryst. Solids, 352, 3121 (2006)
9. M. Scagliotti, M. Villa and G. Chiodelli, J. Non-Cryst. Solids, 93, 350 (1987)
10. M. A. Karakassides, A. Saranti, I. Koutselas, J. Non-Cryst. Solids, 347, 69 (2004)
11. J. E. Pemberton, L. Latifzadeh, J. P. Fletcher, S. H. Risbud, Chem. Mater., 3, 1995 (1991)
12. A. Bertoluzza, M. A.Battaglia, R. Simoni, D. A. Long, J. Raman Spectrosc., 14, 178 (1983)
13. G. B. Rouse Jr., P. J. Miller and W. M. Risen, J. Non-Cryst. Solids, 28, 193 (1978)
14. N. Nelson and G. J. Exarhos, J. Chem. Phys. 71,2739(1979)

STUDIA UNIVERSITATIS BABEŞ-BOLYAI, PHYSICA, LI, 2, 2006

THE PRODUCTION AND CHARACTERIZATION OF SOME MEDICALLY USED RADIOISOTOPES

LAURA DARABAN, O. COZAR, L. DARABAN*,

ABSTRACT. The isotopic neutron sources of ^{241}Am-^{9}Be and ^{239}Pu-^{9}Be and the cyclotron were used for the production of some medical interest radioisotopes such as: ^{116m}In,^{56}Mn, ^{198}Au, ^{61,64}Cu. The ^{64}Cu radioisotope is both a beta and a positron emitter, being used for labelling of PET imaging radiopharmaceuticals. This radioisotope was also obtained by irradiation of ^{64}Zn target at a Scanditronix MC40 cyclotron with a 19.5 MeV deuteron beam energy. All produced radioisotopes were analysed by γ-spectrometry with Ge-Li detectors.

Keywords: Radioisotopes, γ-spectrometry, neutron sources, cyclotron, PET, radiotherapy.

1. Introduction

Radionuclides are often used for imaging and as tracers to study processes in a wide variety of fields. In particular, they are commonly applied in diagnostic medicine, clinical chemistry, molecular biology, and research in the natural and life sciences [1]. A well-known PET radioisotope is ^{64}Cu, which is both a positron and a beta emitter, and is already used for labeling of some radiopharmaceuticals for PET imaging, as well as for systemic radiotherapy and radionuclide immunotherapy of tumours.

One of the most used method of producing radioisotopes is that of irradiation with neutrons obtained from isotopic neutron sources of (α, n) type [2, 3]. The performance in radionuclides production is about 10^3- 10^6 times lower than in the case of the nuclear reactor. The productivity of some important neutron nuclear reactions is given, [4], in Table 1:

---

* Faculty of Physics, Babes- Bolyai University, Cluj- Napoca, Romania

Table 1.

The specific activity of some medically used radioisotopes

Radionuclide	**Nuclear reaction**	**Main γ- emission (keV) and Abundance (%)**	**Specific activity at saturation (Ci/g)**
^{198}Au $T_{1/2}$ = 2.70 d	^{197}Au(n,γ)^{198}Au	411.80 (96)	8
^{56}Mn $T_{1/2}$ = 2.58 h	^{55}Mn(n,γ)^{56}Mn	846.77 (98.9) 1810.77 (27.2) 2113.12 (14.3)	3.9
^{116m}In $T_{1/2}$ = 54 min	^{115}In(n,γ)^{116m}In	416.86 (27.7) 818.71 (11.5) 1097.32 (56.2) 1293.55 (84.4) 1507.67 (10.0)	21
^{64}Cu $T_{1/2}$ = 12.70 h **^{66}Cu** $T_{1/2}$ = 5.15 min	^{63}Cu(n,γ)^{64}Cu ^{65}Cu(n,γ)^{66}Cu	1345.84 (0.473) 1039.23 (9.0)	0.79

The cyclotron production methods of radioisotopes with medical applications have been studied by several groups [1, 5-7]. Among other possible methods for cyclotron production of ^{64}Cu, together with the short-lived positron emitter ^{61}Cu ($T_{1/2}$ = 3.4h), deuteron irradiation of zinc of natural isotopic composition via the (d,αn) and (d,2pn) nuclear reactions has been studied. The experimental excitation functions for deuteron irradiation of natural zinc targets have been also measured in the energy range of 10 to 19 MeV [1]. Table 2 shows the main nuclear reactions induced by deuterons in natural zinc including the calculated thick target yields of the corresponding radioisotope [5, 6]. As indicated in Table 2, deuteron irradiation of natural zinc leads to the simultaneous production of both Cu and Ga radioisotopes.

Table 2.

Main nuclear reactions induced by deuterons in natural zinc target together with the γ-emissions energies and intensities of the produced radionuclides [1]

Radioisotope	Nuclear reaction	Main γ-emission (keV) and Abundance (%)	Thick target yield (MBq/μA.h)
^{64}Cu $T_{1/2}$ = 12.70 h	^{64}Zn(d,2p) ^{66}Zn(d,α) ^{67}Zn(d,αn) ^{68}Zn(d,α2n)	1345.84 (0.473)	14.12 8.60 3.36 0.01 sum: 26.09
^{61}Cu $T_{1/2}$ = 3.33 h	^{64}Zn(d,αn)	656.01 (10.77)	179.20
^{67}Ga $T_{1/2}$ = 3.26 d	^{66}Zn(d,n) ^{67}Zn(d,2n) ^{68}Zn(d,3n)	184.58 (21.2) 300.22 (16.8) 393.53 (4.68)	15.28 3.78 0.21 sum: 19.27
^{66}Ga $T_{1/2}$ = 9.49 h	^{66}Zn(d,2n) ^{67}Zn(d,3n)	833.50 (5.896) 1039.35 (37.00)	109.12 0.29 sum: 109.41
^{69m}Zn $T_{1/2}$ = 13.76 h	^{68}Zn(d,p) ^{70}Zn(d,pn)	438.63 (94.77)	28.06
^{65}Zn $T_{1/2}$ = 244.26 d	^{64}Zn(d,p) ^{66}Zn(d,p2n) ^{64}Zn(d,n)+ decay	1115.55 (50.6)	0.29 ~ 0 ~ 0 sum: 0.29

2. Experimental

The irradiation block used for the neutron activation has two isotopic neutron sources of $^{241}Am-^{9}Be$ and $^{239}Pu-^{9}Be$ with a fluence of $1.1\cdot10^{7}$ n/s and $5.5\cdot10^{7}$ n/s respectively. These two sources are introduced in a closed-end tube, which is placed inside a paraffin block. The function of the pure paraffin block is to slow down the neutrons through multiple collisions with the hydrogen atoms. The so called “slowed down” neutrons end up in the lateral channels, where our samples are set. The gamma spectra of the obtained radioisotopes were acquired using a Ge(Li) detector KOVO type, coupled to a multichannel analyzer ICA-80 type. The calibration in efficiency was made using a ^{226}Ra source with an activity of 3.33 kBq (Fig.1). This made possible an accurate determination of the radioisotopes peak energies and therefore, the identification of their disintegration schemes.

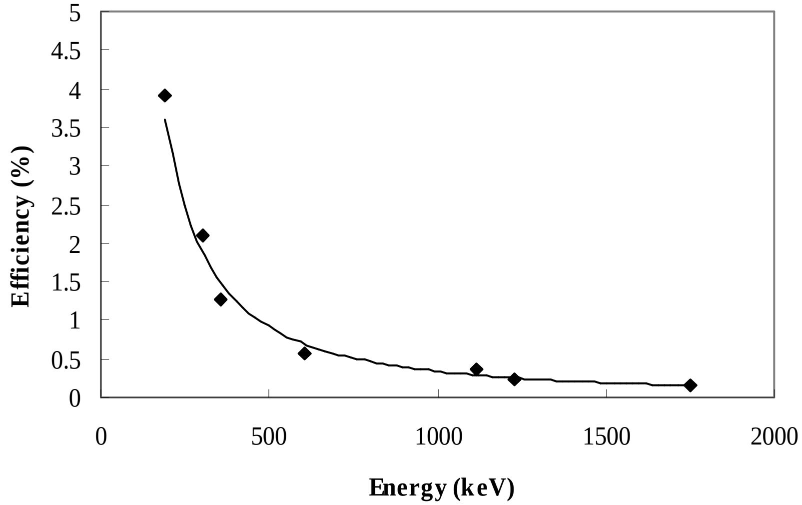

Fig.1. The efficiency curve of Ge(Li) detector

In the case of the ^{64}Cu production by deuteron irradiation at the Joint Research Centre Cyclotron in Ispra, Italy, a stack of 5 foils of ^{64}Zn of 14 ± 0.50 µm thickness together with the Ti monitor was prepared. In order to avoid any losses of activity by recoil processes, each of the foils was enveloped in a catcher foil of pure Al of 22.5 ± 1 µm thickness. The irradiation of the stack was carried out at the Scanditronix MC 40 cyclotron for about 3 h at a very low beam current in order to prevent any significant heating of the foils. The activities produced in the irradiated foils were assessed by using high-resolution γ-spectrometry with a HPGe detector, calibrated in energy at efficiency by using two certified standard ^{152}Eu sources (of 1µCi and 10µCi) at different geometries from the Ge crystals.

3. Results and discussion

Using neutron isotopic sources of Am-Be and Pu-Be, with a total fluence of $6.6 \cdot 10^7$ n/s, the following nuclear reactions were studied: ^{197}Au(n,γ)^{198}Au, ^{115}In(n,γ)^{116}In, ^{55}Mn(n,γ)^{56}Mn, ^{63}Cu(n,γ)^{64}Cu, ^{65}Cu(n,γ)^{66}Cu. The samples containing the target isotopes were irradiated by the neutron sources and the γ-spectra of the produced radioisotopes were then acquired. By analyzing each peak energy on the spectra, it can be determined the type of the new produced radioisotope.

It was also taken in account the disintegration curve, which provides the half-life of the formed radioisotopes, especially in the case of copper isotopes, when some interferences appear on the same peak such as the annihilation peak at 511 keV (Fig.2).

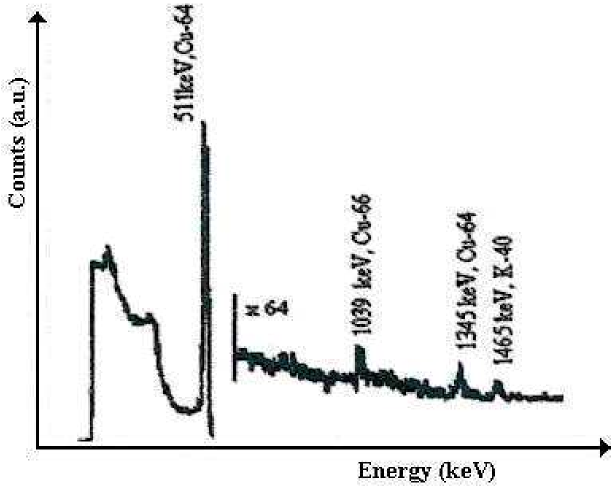

Fig.2. Characteristic gamma spectrum of ^{64}Cu

The appearance of the 511 keV annihilation peak on the γ-spectrum of the studied sample, clearly shows that it contains the ^{64}Cu radionuclide. The weak peak from 1345 keV corresponds also to ^{64}Cu from the reaction ^{63}Cu(n,γ)^{64}Cu with half-life of 12.7 h. Another weak peak on the spectrum from 1039 keV is due to ^{66}Cu from the reaction ^{65}Cu(n,γ)^{66}Cu with a short half-life of 5.15 min. By processing our data (Fig.3), we obtained a half-life of 12.83 h for ^{64}Cu in agreement with the theoretical half-life of 12.7 h [8].

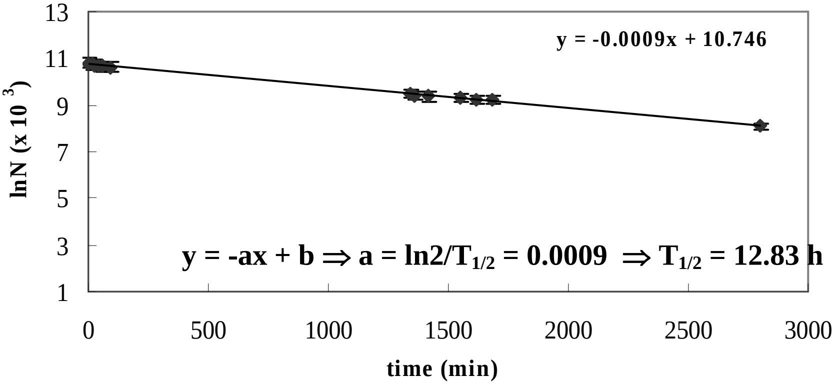

Fig.3. Decay time estimation for ^{64}Cu

In order to produce ^{64}Cu used for PET experiments with high specific activity, deuteron irradiation on enriched zinc targets has been performed at a cyclotron. The experimental excitation functions for the ^{64}Zn(d,2p)^{64}Cu reaction up to 19.5 MeV deuteron energy by using the stack foil technique, were measured. The γ-spectrometry was used to measure qualitatively and quantitatively activities of the various produced radioisotopes (Fig.4). In all the acquired γ-ray spectra, the γ-peak of ^{64}Cu had a statistical counting uncertainty not greater than 5 %.

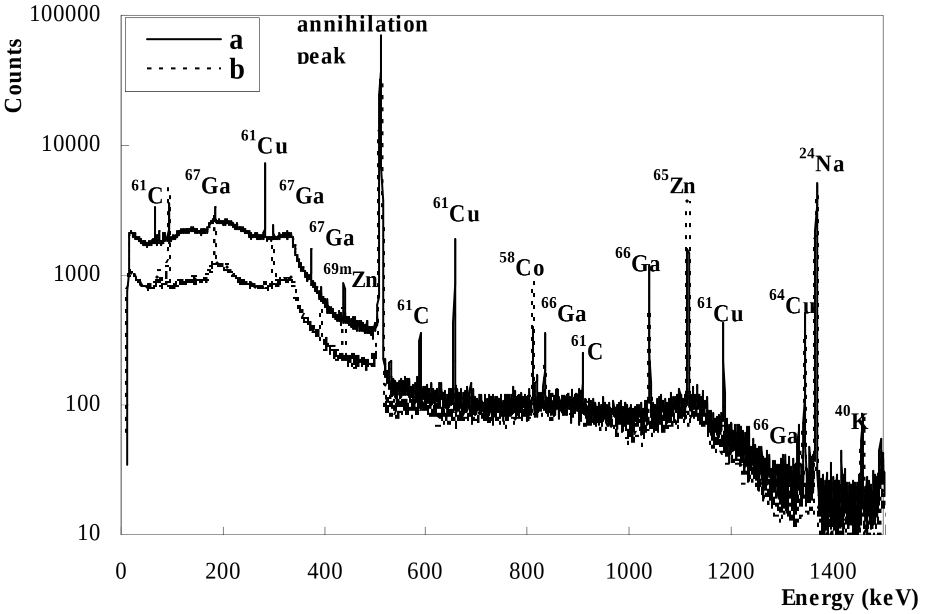

Fig.4. Two γ-ray spectra of an activated ^{64}Zn foil acquired twice after one day (a) and after two days (b) respectively from the end of irradiation

Two typical γ-ray spectra of an activated ^{64}Zn foil together with the enveloping Al foils acquired twice after one day (spectrum a) and after two days (spectrum b) respectively from the end of the deuteron irradiation (Fig.4). The γpeak of ^{64}Cu (1345.84 keV) together with those of ^{61}Cu (282.96, 656.01, 1185.23 keV) are well resolved.

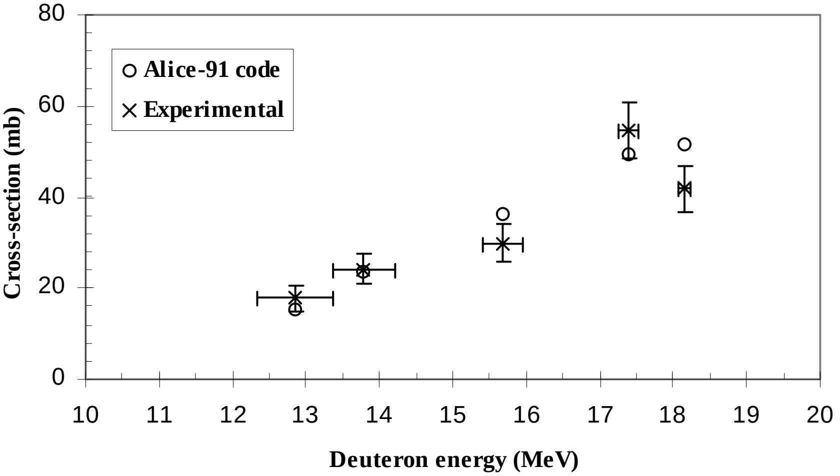

Fig.5. Measured excitation function of the ^{64}Zn(d,2p)^{64}Cu reaction

The excitation function of the reaction ^{64}Zn(d,2p)^{64}Cu in the deuteron energy range below 19.5 MeV is shown in Fig.5. The cross-section uncertainties were determined by considering uncertainties of ^{64}Cu measured activities and deuteron integrated beam current. The different deuteron energy uncertainties have been calculated using SRIM 2003 code [9] by taking into account thickness uncertainties of the different foils of the stack. The theoretical function calculated with the Alice-91 code is also shown for comparison. The theoretical and experimental functions are in good agreement. As predicted by theory, the thick target yields of ^{64}Cu in the cases of deuteron irradiation of natural Zn or of enriched ^{64}Zn samples are only slightly different and are in good agreement with values reported in the literature [1, 6] for deuteron irradiation of natural Zn. The advantage of using enriched ^{64}Zn as target material is that simultaneous Ga radioisotope production (Fig.4) is practically avoided [5].

4. Conclusions

In this paper it is shown that by using the isotopic neutron sources some radioisotopes with great importance in nuclear medicine such as: ^{116m}In, ^{198}Au, ^{56}Mn, ^{64}Cu, could be produced in local physical and clinical laboratories. This is a great advantage by taking into account their short half-life and the transport difficulties. Each radioisotope is characterized by its gamma spectrum, half-life and the desintegration scheme. The productivity of these radiosotopes by irradiation with isotopic neutron sources is low, approximatively 0.2 μCi, but is relatively good for laboratory measurements.

For medical investigations it is recomanded the production of radiosotopes at the cyclotron, as ^{64}Cu for example, produced by irradiation on enriched ^{64}Zn targets with deuterons.

The production of ^{64}Cu and its experimental excitation functions via the ^{64}Zn(d,2p)^{64}Cu reaction, determined by the stack foil technique on enriched ^{64}Zn material are in good agreement with theoretical curves and with previously reported results on deuteron irradiation of natural Zn.

Acknowledgments

The first author kindly acknowledges the financial support through the Marie-Curie Fellowship for this project (contract number HPMT-CT-2001-00362) by the European Commission through the Institute of Health and Consumer Protection of the Joint Research Centre, Ispra, Italy and to dr. Kamel Abbas for useful discussions and facilities to work in the cyclotron laboratories.

REFERENCES

1. M.L. Bonardi., F. Groppi, C. Birattari, L. Gini, C. Mainardi , A. Ghioni, E. Menapace, K. Abbas, U. Holzwarth, M.F. Stroosnijder , *J.Radioanl. Nucl. Chem.*, **257**, 229, (2003).
2. D. De Soete, E. Gijbels, J. Hoste, *Neutron Activation Analysis*, p. 123, Wiley-Interscience, London, New York, Sydney, Toronto, 1972.
3. I.E. Teodorescu, *Generatoare de neutroni. Principii şi utilizari*, p.352, Ed. Academiei Române, Bucureşti, 1969.
1. P. Sandru, Aurelia Topa, *Radionuclizii*, p.83, 93, Ed. Academiei Romane, 1968.
4. K. Abbas, J. Kozempel, M. Bonardi, F. Groppi, A. Alfarano, U. Holzwarth, F. Simonelli, H. Hofman, W. Horstmann, E. Menapace, L. Leseticky and N. Gibson, J. *Appl. Radiat. Isot*., **64**, 1001, (2006).
5. F. Tarkanyi, S. Takacs, F. Ditroi, A. Hermanne, M. Sonck, Y. Shubin*, Nucl. Instr.& Meth. in Physics Research* ***B*** **217**, 531, (2004).
6. F. Szelecsenyi, G.F. Steyn, Z. Kovacs, T.N.van der Walt, K. Suzuki, K. Okada, K. Mukai, *Nucl. Instr.& Meth. in Physics Research* ***B*** **234**, 375, (2005).
7. R. B. Firestone, L.P. Ekström, *Table of Isotopes*, New York, USA, 1998.
8. J.F. Ziegler, 2003, *SRIM 2003 code*. Available from www.srim.org.

STUDIA UNIVERSITATIS BABEŞ-BOLYAI, PHYSICA, LI, 2, 2006

MAGNETIC FIELD SIMULATION FOR MOUSE® DESIGN USING VECTOR FIELDS™ OPERA 3D

L. SZABÓ[1], A. PÎRNĂU[1,3], A. VODĂ[2], B. BLÜMICH[2], O. COZAR[1]

ABSTRACT. Mobile nuclear magnetic resonance deals with unilateral sensors like the NMR-MOUSEÂ to investigate materials non-destructively.

New NMR MOUSE designs require combinations of magnets for which the spatially field distribution is too complex to be computed by hand. The numerically simulations of these new configurations are needed in order to predict a good result. A commercial software Vector Fields OPERA has been used to perform the simulations. The NMR-MOUSE® is aesred trademark of RWTH Aachen.

Introduction

In this work have been used already known MOUSE designs [1] as the simplest bar magnet [2] and U-shape magnet [3]. These type of magnets have a well defined sensitive volume and field gradient. If the sample to investigate consists in a iron plate (core) coated with a polymer layer, the iron part of the sample destroys the original field distribution and so, the sensitive volume and filed gradient are completely changed. This is one of the facts which is leading us to the idea to simulate the interaction of the magnetic field given by the existing magnets with different types of iron bodies placed near the magnets. Moreover, iron bodies placed in a proper position can improve the homogeneity of the field which is desired for NMR measurements of transverse relaxation time but also in other geometric conditions, can give a well defined and strong field gradient, which is useful for imaging and diffusion measurements.

The simulations have been done for three different iron bodies: plate, disk and cylinder. The distance between the body and the magnet has been changed and also the body dimensions. All the results have been compared and can represent a starting point in a new type of MOUSE system [4].

Homogeneous fields, the challenge of maximizing the sensitivity for thin samples, seem to have been neglected. The non-destructive investigation of arbitrarily large objects, membranes, paper, coatings, and surface layers from polymer aging and degradation are examples of thin objects of technical interest for analysis by NMR [5].

---

[1] Babeş-Bolyai University, Faculty of Physics, Kogălniceanu 1, RO-400084 Cluj-Napoca, Romania
[2] Institute of Technical Chemistry and Macromolecular Chemistry, RWTH Aachen, Germany
[3] National Institute for R&D of Isotopic and Molecular Technology, P.O. Box 700, RO-400293 Cluj-Napoca, ROMANIA Address for correspondence: szabolaci81@yahoo.com

Theoretical aspects

1. The Finite Element Method

The Finite Element method is used to obtain solutions to partial differential or integral equations that cannot be solved by analytic methods. Partial differential and integral equations describe the spatial and temporal variation of a field either directly in terms of the field variable, for example the magnetic flux density B, but more often using a potential function that is related to the field by a gradient (∇) or (∇_x) operation. The finite element method is generally applicable to any problem with any type of non-linearity. The method is based on division of the domain of the equation (volume of space in which the equation is satisfied) into small volumes (the finite elements). Within each finite element a simple polynomial is used to approximate the solution.

The concepts used in finite element analysis are independent of the number of space dimensions, however it is convenient to use a simple one space dimension problem in order to make the algebra straightforward and explanatory diagrams easy to view.

A Newton-Raphson method can be used to solve this type of non-linear equation. Given an initial solution Φ_n a new solution Φ_{n+1} is found by solving the linearized Jacobean system[1]:

$$\Phi_{n+l} = \Phi_n - J_n^{-1} - R_n \qquad (1)$$

where the residual *R* is given by

$$R_n = K_n\Phi_n - S_n \qquad (2)$$

and the Jacobean *J* by

K$_n$ is a coefficient matrix; **S$_n$** the known right hand side vector

$$J_n = \frac{\partial}{\partial\Phi_n}\left(K_n\Phi_n - S_n\right) \qquad (3)$$

This method converges providing the initial approximation used to start the iteration is not too far from the real solution. As it approaches the solution its convergence becomes quadratic. In the context of non-linear finite element solutions to the electromagnetic field equations the reliability of the Newton-Raphson method is strongly linked to the smoothness of the equation used to relate the permeability or permittivity to the field.

To aid convergence, when the material property curve is not smooth or when the initial solution is far from the final solution, a relaxation factor is used in equation 1, which becomes:

$$\Phi_{n+l} = \Phi_n - \alpha J_n^{-1} - R_n \qquad (4)$$

Where α is chosen, starting with 1 and multiplying by 2 (if the change in |R| is too small) or dividing by 2 (if the norm of the residual $|R_{n+1}|$ would be greater than $|R_n|$) to find the value which minimizes the norm of the residual $|R_{n+1}|$ at the start of the next iteration.

The local error at a point within a finite element model is strongly linked to the size of the elements surrounding the point and weakly linked to the average element size over the whole space, although this second source of error becomes more important and less easily estimated in non-linear solutions. The relationship between the local error in the solution and the surrounding elements' size is given by:
For linear shape functions

$$E(\Phi) = O(h^2) \quad (5)$$

and for quadratic shape functions

$$E(\Phi) = O(h^3) \quad (6)$$

where E is the error, O means 'of the order' and h is the linear dimension of the elements. This simple analysis is only true for square elements, but it is reasonable to assume the worst case and use the largest dimension for h.

2. The TOSCA Algorithm

TOSCA can be used to compute current flow, magnetostatic or electrostatic fields, including the effects of non-linear average in three dimensions. The program incorporates state of the art algorithms for the calculation of electromagnetic fields, advanced finite element and non-linear equation numerical analysis procedures. In the following sections, the algorithms used in TOSCA are described so that users are able to relate the finite element model to their application problem.

Three dimensional stationary electromagnetic fields can be represented as the sum of a solenoidal field and a rotational field. In electrostatic fields there is never a rotational component, the field can therefore always be defined using the electrostatic potential (V). The electric field intensity (E) is given by:

$$E = -\nabla V \quad (7)$$

The following relation exists also between the divergence of the electric flux density (D) and the charge density (ρ):

$$\nabla \bullet D = \rho \quad (8)$$

Combining equations 7 and 8 and introducing the dielectric permittivity tensor (ε) the usual Poisson's equation description of the electrostatic potential results:

$$\nabla \bullet \varepsilon \nabla V = -\rho \text{, where } D = \varepsilon E. \tag{9}$$

A similar equation arises for current flow problems,

$$\nabla \bullet \sigma \nabla V = 0 \tag{10}$$

where σ is the conductivity, and $J = \sigma E$.

Stationary magnetic fields, in general consist of both solenoidal and rotational components. The field produced by electric currents has a rotational component inside the volumes where the currents flow. In the external space the field is solenoidal but the scalar potential is multi-valued. The field produced by magnetized volumes is solenoidal. It is convenient to use a splitting of the total field into two parts in order to obtain a description of the field in terms of a simple scalar potential.

The total field intensity H is defined using the reduced field intensity (H_m) and the conductor field intensity (H_s):

$$H = H_m + H_s \tag{11}$$

The reduced field intensity can now be represented using the reduced scalar potential (ф):

$$H_m = -\nabla \phi \tag{12}$$

and in the case of stationary magnetic fields where the exciting currents are prescribed, the conductor field intensity may always be directly evaluated by integration:

$$H_s = \int_{\Omega_J} \frac{J \times R}{|R|^3} d\Omega_J \tag{13}$$

The divergence of the flux density is always zero. Introducing the permeability tensor (μ) and combining eqs. 11 and 13 gives the partial differential equation for the reduced scalar potential (ф):

$$\nabla \cdot \mu \nabla \phi - \nabla \cdot \mu \left(\int_{\Omega_J} \frac{J \times R}{|R|^3} d\Omega_J \right) = 0 \tag{14}$$

Boundary conditions are used in two ways. Firstly they can provide a way of reducing the size of the finite element representation of symmetrical problems. Secondly they are used to approximate the magnetic field at large distances from the problem (far-field boundaries).

Table 1.
Boundary Conditions

Magnetic Fields	Field Symmetry	Scalar Potential
TANGENTIAL MAGNETIC	$H \cdot n = 0$	$\frac{\partial \phi}{\partial n} = 0$
NORMAL MAGNETIC	$H \times n = 0$	ϕ=*constant*

The symmetry of the fields are implied by the potential boundary conditions applied to the finite element model. The simplest types of boundary condition are shown in Table 1 where n is the normal unit vector to the considered surface. Note that in this table, (ф) refers to either the reduced or total scalar potential. Boundary conditions on the reduced scalar potential only affect the reduced field intensity.

Results and Discussion

1. Bar magnet and plates

The magnetic field simulations for a bar magnet [2] and an iron plate at different distances between them have been done. Also different plate sizes have been used, as different plate thickness. The bar magnet has a height and a diameter of 50 mm. All the simulated field values are presented here as magnitude, which value is almost equal in this case with the z component of the field. In Fig. 1 we plot the field profiles along z axis for the 50*50 mm^2 plate and 2 mm thickness, for different positions relative to the top of the bar magnet. It can be clearly seen that the field is stronger for a small distance and decreases with increasing the distance. But the gradient of the field is evolving in other direction, it is bigger for the case of a large distance. So far, we see a field homogeneity tendency by placing an iron plate close to the bar magnet. By increasing the plate thickness we not observe a significant change in the field profiles (Fig. 2). In Fig. 3 can be seen the field profiles comparison for two plate thickness with 50*50 mm^2 in size. Increasing the size of the plate, we do not see a significant effect. By decreasing the plate size, the filed starts to change dramatically, due to the loss of the force lines intersections with the iron medium (Fig. 4). Again, the profile is not changing but the field strength increases by increasing the thickness, as it is expected. The maxima of the field values for all the cases are shown in Fig. 5. In Fig. 6 it can be seen the field profiles comparison for two plate thickness with 10*10 mm^2 in size.

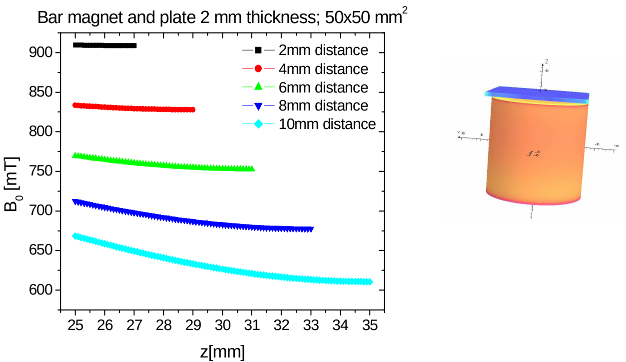

Fig. 1. Bar magnet and plate 2 mm thickness, 50x50 mm^2.

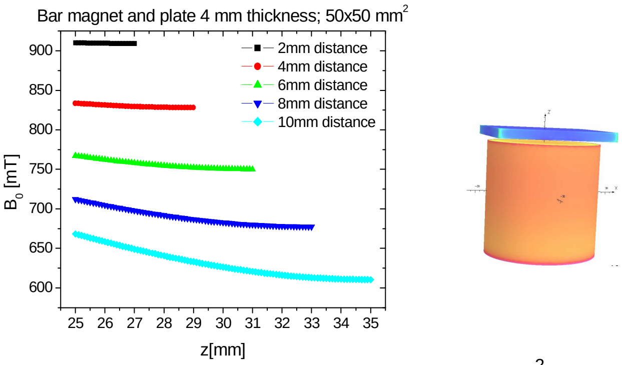

Fig. 2. Bar magnet and plate 4 mm thickness, 50x50 mm^2.

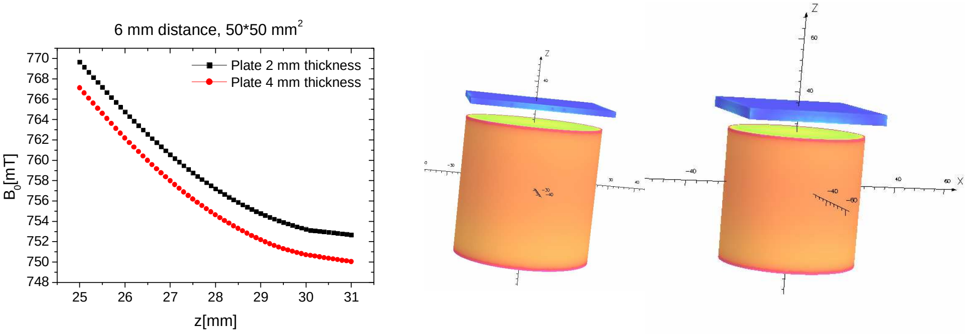

Fig. 3. Comparison between plate 2 mm and 4mm thickness, 6 mm distance.

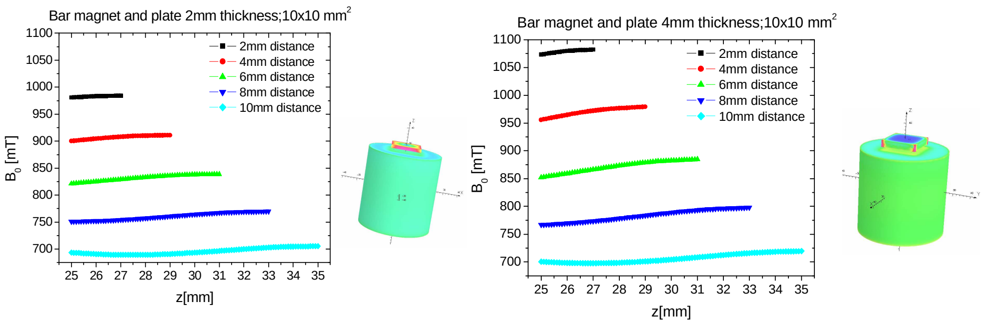

Fig. 4. Bar magnet and plate 2 mm and 4 mm thickness, 10x10 mm^2.

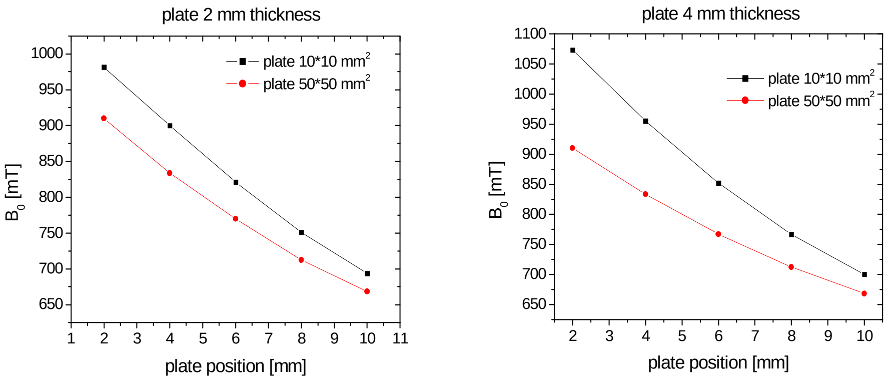

Fig. 5. The maxima of B_0 for 2 mm and 4 mm thickness plates.

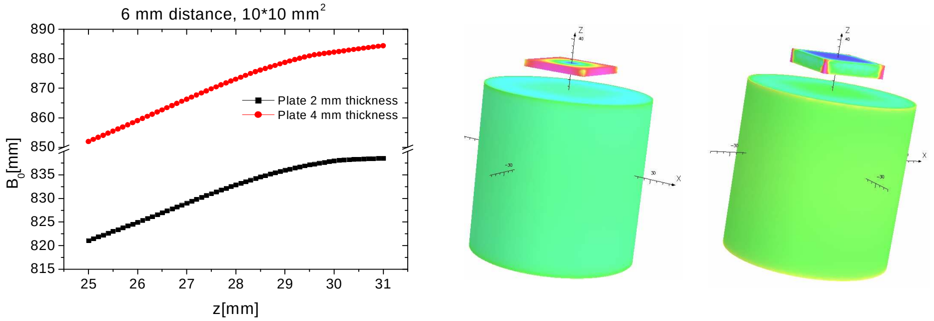

Fig. 6. Comparison between plate 2 mm and 4mm thickness, 6 mm distance.

2. Bar magnet and disks

The magnetic field simulations for a bar magnet and an iron disk at different distances between them have been done. Also different disk sizes have been used, as different disk thickness. The bar magnet has a height and a diameter of 50 mm. All the simulated field values are presented here in magnitude, with values almost equal with the z component of the field. In Fig. 7 and Fig. 8 we plot the field profiles along z axis for the 50 mm diameter disk and 2 mm(6 mm) thickness, for different positions relative to the top of the bar magnet. It can be clearly seen that the field is stronger for a small distance and decreases with increasing the distance. But the gradient of the field is evolving in other direction; it is bigger for the case of a large distance. So far, we see a field homogeneity tendency by placing an iron disk close to the bar magnet. By increasing the disk thickness we not observe a significant change in the field profiles Fig. 8. Also, increasing the size of the disk, we do not see a significant effect. The maxima of the field values for all cases are shown in Fig. 9. In Fig. 10 the comparison between the plate and disk is shown. The field strength is larger in the case of a plate and the profiles are the same. The changes in the field strength are due only to a bigger surface of the iron, normal to the field lines.

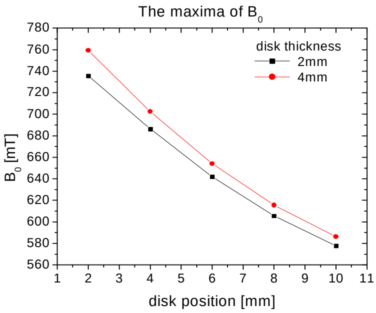

Fig. 9. Maxima of B_0 for 2 mm, 4 mm, and 25 mm diameter disks.

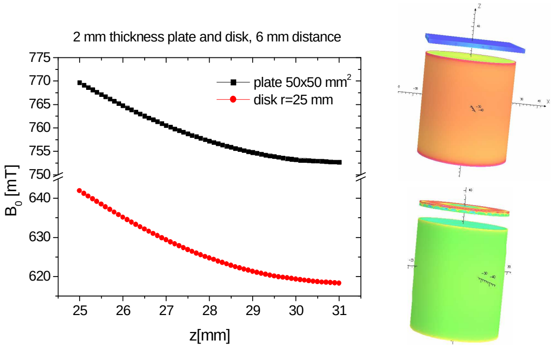

Fig. 10. Comparison between plate and disk 2 mm thickness, 6 mm distance.

3. U shape magnet and yoke

The magnetic field of the U-shape type magnet [3] has been analyzed in the presence of an iron yoke placed between the two magnets. Different yoke sizes and z positions (see Fig. 11, 12 and 13) have been tried. The main conclusion of this part is the difference in the field gradient.

This can be exploited for the imaging techniques in inhomogeneous magnetic fields for specific measurements.

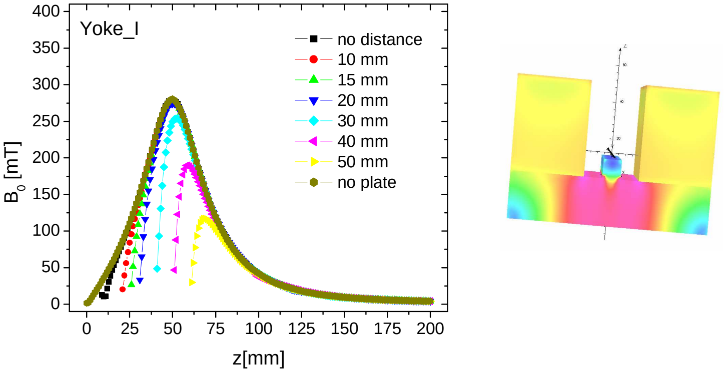

Fig. 11. U shape magnet and yoke I

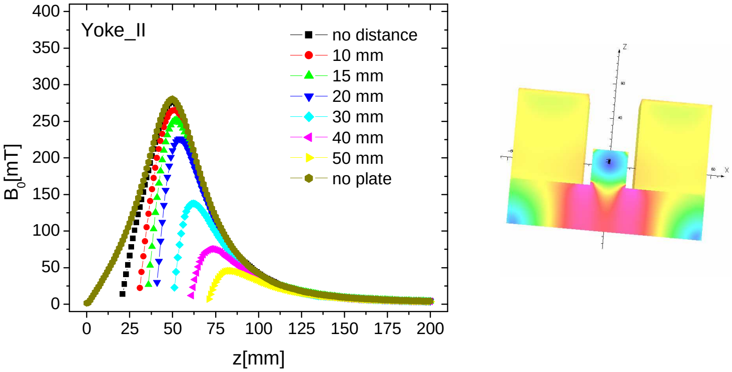

Fig. 12. U shape magnet and yoke

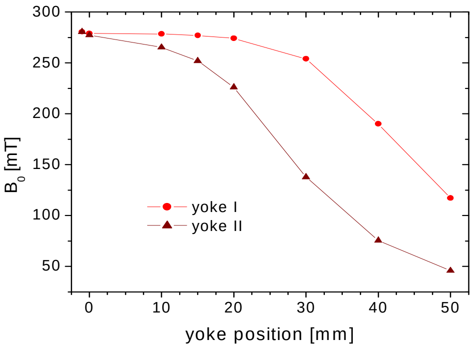

Fig. 13. The maxima of B_0 for U shape magnet and yoke

Conclusion

The numerically simulations of these new configurations are studied in order to predict better results.

The field strength is bigger in the case of a plate and the profiles are the same. The changes in the field strength are due only to a larger surface of the iron, normal to the field lines.

The profile is not changing but the field strength increases by increasing the thickness.

The main conclusion of this part is the difference in the field gradient. This can be exploited for the imaging techniques in inhomogeneous magnetic fields for specific measurements.

All the results have been compared and can represent a starting point in a new type of MOUSE system.

REFERENCES

1. B. Blümich, F. Casanova, J. Perlo, S. Anferova, V. Anferov, K. Kremer, N. Goga, K. Kupferschläger, M. Adams, Advances of Unilateral, Mobile NMR in Nondestructive Materials Testing, Magn. Reson. Imag. 23,197 (2005).
2. Blümich B, Anferov V, Anferova S, Klein M, Fechete R, Adams M, et al. A simple NMR-MOUSE with a bar magnet. Magn Reson Eng, 15, 255 (2002).
3. J. Perlo, F. Casanova, B. Blümich, 3D imaging with a single-sided sensor: an open tomograph, J. Magn. Res. 166, 228 (2004).
4. G. Eidmann, R. Savelsberg, P. Blümler, B. Blümich, The NMR MOUSE: A Mobile Universal Surface Explorer, J. Magn. Reson. A 122, 104 (1996).
5. Casanova F, Perlo J, Blqmich B, Kremer K. Multi-echo imaging in highly inhomogeneous magnetic fields. J Magn Reson. 166, 76 (2004).

STUDIA UNIVERSITATIS BABEŞ-BOLYAI, PHYSICA, LI, 2, 2006

THE STRUCTURE OF CuO – P_2O_5 – CaF_2 GLASS SYSTEM

N. VEDEANU*, O. COZAR, I. ARDELEAN, D. A. MAGDAS

ABSTRACT. XCuO(1-x)[P_2O_5•CaF_2] glass system with $0 \leq x \leq 20$%mol was prepared and investigated by means of Raman and EPR spectroscopy in order to evidence the structural changes induced by the copper oxide in different ratio and its modifier role.

Raman spectra of the studied glasses contain the typical bands attributed to the phosphate glasses. It can be observed that the band at ~1020 cm^{-1} attributed to PO_2 and PO_3 groups increase in intensity as the phosphate chain breaks and so a bigger number of PO_2 and PO_3 are formed. The bands at ~1170 cm^{-1} and 1270 cm^{-1} belonging to the symmetric and asymmetric stretching vibrations in PO_2 groups decrease in intensity with increasing the CuO content and this fact is consistent with the depolymerization of the three dimension phosphate network.

EPR results obtained for copper doped glasses show $g_\perp < g_\parallel$ indicating tetragonally elongated octahedral sites for Cu^{2+} ions. With the increase of CuO content ($x \geq 20$ mol%) the spectrum becomes a broad line with $\Delta B \sim 300$ Gs typical for clustered ions.

Introduction

Copper – doped phosphate glasses have interesting electrical and optical properties that make them suitable for the use as super – ionic conductors, solid state lasers, color filters or non-linear optics [1]. The technological importance of these glasses requires a detailed understanding of the molecular and structural chemistry in order to be designed for particular applications.

Previous studies [2] made on simple binary copper phosphate glasses with various [Cu^{2+}] ratio had shown that the properties of these glasses depend on this ratio as it induces a variation in the glass structure [3]. The effect of [Cu^{2+}] ratio could not be observed by IR and NMR analysis, but changes in depolymerization of the phosphate chain can be observed by Raman scattering [4].

This paper presents the results of Raman and EPR spectroscopy for Cu^{2+} ions in xCuO(1-x)[P_2O_5•CaF_2] glass system. The interest lies on the nature of the ground state of the paramagnetic ions, their local symmetry and also on their modifier role in the paramagnetic network.

---

* Babes-Bolyai University, Department of Biomedical Physics, 400084 Cluj-Napoca, Romania nvedeanu@phys.ubbcluj.ro

Experimental

In order to prepare xCuO(1-x)[P_2O_5.CaF_2] glasses with 0 ≤ x ≤ 20 mol% we used $(NH_4)H_2PO_4$, CuO and CaF_2 of reagent grade purity. The samples were prepared by weighting suitable amounts of these components, powder mixing and mixture melting in a sintered corundum crucibles at 1250 ^oC for half an hour. The mixture was put into the furnace directly at this temperature. The melts were poured then on stainless steel plates.

EPR measurements were performed at 9.4 GHz (X-band) at room temperature using a JEOL-JES 3B equipment.

Raman spectra were measured on an Olympus BX-41 Jobin Yvon Horiba with Peltier CCD cooling, using an excitation source of 632,8 nm from a He-Ne laser.

Results and Discussion

A. Raman data

Raman spectra of xCuO(1-x)[$P_2O_5 \cdot CaF_2$] glass system with 0 ≤ x ≤ 20 mol% are given in Fig. 1. The main bands observed in the spectra are: ~ 350 cm^{-1}, ~ 720 cm^{-1}, ~ 980 cm $^{-1}$, 1100 cm^{-1}, ~ 1140 cm^{-1} and ~ 1280 cm^{-1}.

The evolution of these bands is influenced by the CuO content. The band at ~350 cm^{-1} is due to the network bending vibrations and also to Cu-O-P vibrations [5, 6]. This band is constant with the rate of the modifier oxide and this shows that PO_4 chains exist in the structure of the glass for both small and high CuO content.

The asymmetric band at ~720 cm^{-1} is attributed to P-O-P in-chains stretching vibrations of the in-chain P-O-P vibration in the long chain phosphate species. The band has a shift of ~ 10 cm $^{-1}$ for x ≥ 20 mol%, due to the change of the in-chain P-O-P bond angle because of CuO effect. A higher wavenumber of this band is a result of a smaller P-O-P bond angle which results from a shorter phosphate chain length due to the depolymerization of the phosphate structure with the addition of Cu^{2+} ions [2].

The band at ~ 980 cm^{-1} belongs to the vibration of PO_3 and PO_2 groups [7]. The band slowly increases in intensity as the phosphate chains breaks and the number of PO_2 and PO_3 groups increase (x ≥ 20 mol%)

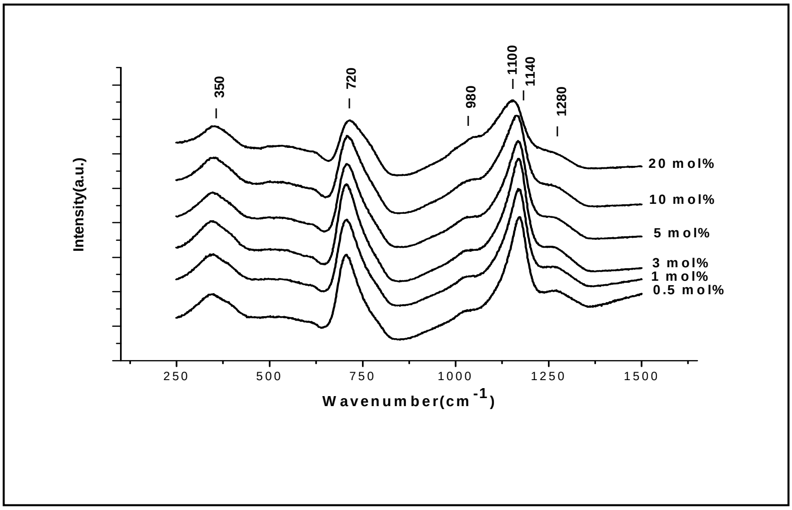

Fig. 1. Raman spectra of xCuO(1-x)[$P_2O_5 \cdot CaF_2$] glass system

The bands at 1140 cm^{-1} and 1280 cm^{-1} belong to PO_2 symmetric and asymmetric stretching vibrations [2, 6]. The decrease in intensity of these two bands with the increase of CuO content is characteristic of phosphate glasses and it is consistent with the depolymerization of the three dimensional network [2]. These two bands are often attributed in literature [6] to some “strained” structures; their presence as distinct bands rather than a broadening of the main band suggests a specific structure. Similar features were found in some borate glasses [8] or in some silicates including those prepared by sol-gel method [9].

B. EPR investigation

EPR spectra of xCuO(1-x)[P_2O_5.CaO] glasses with $0 \leq x \leq 20$ mol% are given in Fig. 2.

The shape of these spectra for $x \leq 10$ mol% are typical for Cu^{2+} isolated ions having a quartet of hyperfine lines in the parallel band. With the increase of CuO content ($x \geq 10$ mol%) the spectra becomes a broad line with $\Delta B \sim 315$ Gs typical for clustered ions [10, 11].

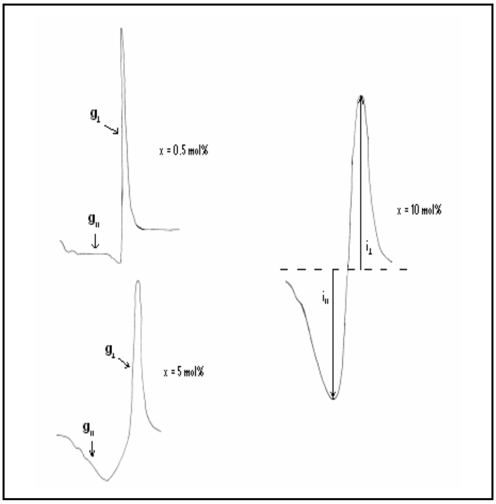

Fig. 2. EPR spectra of $xCuO(1-x)[P_2O_5 \cdot CaO]$

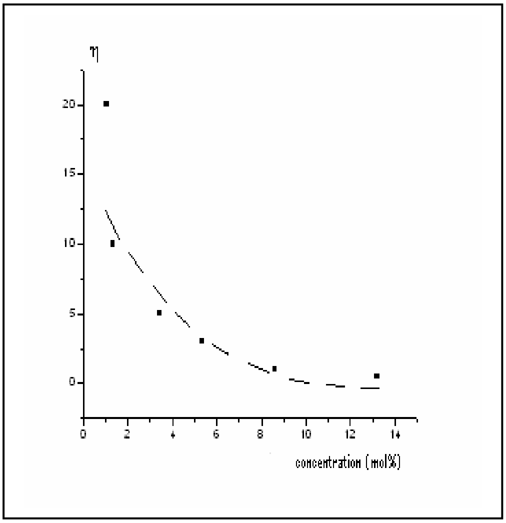

Fig. 3. The composition dependence of glasses EPR lineshape asymmetry for the Cu^{2+} clustered ions

The spin Hamiltonian parameters evaluated from the observed spectra [7, 13, 14] they are in Table 1.

It can be seen that $A_{\parallel}$ and $g_{\parallel}$ values are very sensitive to glass composition suggesting the modification of the local environment of Cu^{2+} ions.

The values obtained at x = 0.5 mol% ($g_\parallel$ = 2.38; $A_\parallel$ = 172,15 10^{-4} cm^{-1}) indicate a hexacoordinated tetragonal symmetry. With the increase of CuO content $g_\parallel$ $A_\parallel$ become 2.44 and 114.77 10^{-4} cm^{-1} respectively for x= 5 mol%. These values are characteristic for tetracoordinated Cu^{2+} ions in tetrahedral local symmetry [15]. In this case the paramagnetic "hole" is not in a pure 3d orbital, but in a state containing an admixture of 3d and 4p orbitals [15].

Tab.1.

EPR parameters for xCuO(1-x)[P_2O_5.CaO] glass system

x mol%	$g_\parallel$	$g_\perp$	$A_\parallel$ 10^{-4} cm^{-1}	α^2	$(\alpha'')^2$
0.5	2.38	2.04	172.15	0.73	0.04
1	2.40	2.04	155.75	0.77	0.04
3	2.42	2.03	127.68	0.81	0.05
5	2.44	2.02	114.77	0.84	0.05

The small values obtained for $A_\parallel$ arises from the contribution of the p-type wave function which has a canceling effect of the d-type wave function, for it always appears with an opposite sign. Thus, a small admixture of $4p_z$ orbital (0.04-0.05, Table 1) in the $3d_{xy}$ ground state leads to a considerable diminishing of the hyperfine splitting [15].

The variation of α parameter for the in-plane σ-bonding ($\alpha^2 \sim 0.77$) indicates a decrease of the covalency degree.

By defining the asymmetry parameter η as the ratio of the heights of $g_\perp$ and $g_\parallel$ absorptions, a decrease of η values can be observed (Fig. 3). This fact is explained by the increasing of the number of Cu^{2+} clustered ions with CuO content.

Conclusions

Raman scattering of copper phosphate glasses is affected by CuO ratio. This is due to the convertion of P-O-P bridging oxygen to P-O-Cu bridging oxygen and in consequence to the depolymerization of the phosphate network that occurs at high rate of Cu^{2+} ions.

EPR analysis indicates a change of the coordination polyhedra for Cu^{2+} ions from a tetragonal to a tetrahedral local symmetry in the studied glasses. For high content of CuO ($x \geq 10$ mo l%) the presence of clustered ions was evidenced from the spectra.

REFERENCES

1. E. Metwalli, M. Karabulut, D. L. Sidebottom, M. M. Morsi, R. K. Brow, J. Non-Cryst. Solids 344, 128 (2004)
2. J. Koo B. S. Bae, H. K. Na, J. Non-Cryst. Solids 212, 173 (1997)
3. B. S. Bae, M. C. Weinberg, Glass Technol. 35, 83 (1994)
4. S. H. Morgan, R. H. Magruder, E. Silberman, J. Am. Ceram. Soc. 70, 70 (1987)
5. M. A. Karakassides, A. Saranti, I. Koutselas, J. Non-Cryst. Solids 347, 69 (2004)
6. J.J. Hudgens, R. K. Brow, D. R. Tallant, S. W. Martin, J. Non-Cryst. Solids 223, 21 (1998)
7. R. Murali, Krishna, J. J. Andre, R. P. Paut, V. P. Seth, J. Non-Cryst. Solids 232-234, 509 (1998)
8. A. K. Hassan, L. M. Torrell, L. Borjesson, H. Doweider, Phys. Rev. B. 45, 12797 (1992)
9. D. R. Tallant, B. C. Bunker, C. J. Brinker, C. A. Balfe, Mater. Res. Soc. Symp. Proc. 73, 261 (1980)
10. F. Gonella, F. Caccavale, L. D. Bogomolova, V. A. Jachkin, Appl. Phys. A 68, 539 (1999)
11. M. V. Ramana, K. Kumar, S. Rahman, D. S. Babu, S. G. Sathyanarayan, G. S. Sastry, j. Mat. Sci. Letters 8, 1471 (1989)
12. O. Cozar, I. Ardelean, J. Non-Cryst. Solids 92, 278 (1997)
13. J. Wong, C. A. Angel, Glass Structure by Spectroscopy, New York, 135 (1976)
14. G. Ramadevudu, M. Shareefuddin, N. S. Bai, M. L. Rao, M. N. Chary, j. Non-Cryst. Solids 278, 205 (2000)
15. O. Cozar, I. Ardelean, V. Simon, L. David, V. Mih, N. Vedeanu, Appl. Mag. Res. 16, 529 (1999)
16. R. Ravikumar, V. Rajagopal Reddy, A. V. Chandrasekhar, B. J. Reddy, Y. P. Reddy, P. S. Rao, J. Alloys and Compounds 337, 272 (2002)

În cel de al LI-lea an (2006) *STUDIA UNIVERSITATIS BABEŞ-BOLYAI* apare în următoarele serii:

matematică (trimestrial)
informatică (semestrial)
fizică (trimestrial)
chimie (semestrial)
geologie (trimestrial)
geografie (semestrial)
biologie (semestrial)
filosofie (semestrial)
sociologie (semestrial)
politică (anual)
efemeride (semestrial)
studii europene (trei apariții pe an)

dramatica (semestrial)
business (semestrial)
psihologie-pedagogie (anual)
ştiințe economice (semestrial)
ştiințe juridice (trimestrial)
istorie (trei apariții pe an)
filologie (trimestrial)
teologie ortodoxă (semestrial)
teologie catolică (trei apariții pe an)
teologie greco-catolică - Oradea (semestrial)
teologie catolică - Latina (anual)
teologie reformată (semestrial)
educație fizică (semestrial)

In the LI-th year of its publication (2006) *STUDIA UNIVERSITATIS BABEŞ-BOLYAI* is issued in the following series:

mathematics (quarterly)
computer science (semesterily)
physics (quarterly)
chemistry (semesterily)
geology (quarterly)
geography (semesterily)
biology (semesterily)
philosophy (semesterily)
sociology (semesterily)
politics (yearly)
ephemerides (semesterily)
European studies (three issues / year)
business (semesterily)

dramatica (semestrial)
psychology - pedagogy (yearly)
economic sciences (semesterily)
juridical sciences (quarterly)
history (three issues / year)
philology (quarterly)
orthodox theology (semesterily)
catholic theology (three issues / year)
greek-catholic theology - Varadiensis (semesterily)
catholic theology - Latina (yearly)
reformed theology (semesterily)
physical training (semesterily)

Dans sa LI-ème année (2006) *STUDIA UNIVERSITATIS BABEŞ-BOLYAI* paraît dans les séries suivantes:

mathématiques (trimestriellement)
informatiques (semestriellement)
physique (trimestriellement)
chimie (semestriellement)
géologie (trimestriellement)
géographie (semestriellement)
biologie (semestriellement)
philosophie (semestriellement)
sociologie (semestriellement)
politique (annuellement)
éphémérides (semestriellement)
études européennes (trois apparitions / année)

dramatica (semestrial)
affaires (semestriellement)
psychologie - pédagogie (annuellement)
études économiques (semestriellement)
études juridiques (trimestriellement)
histoire (trois apparitions / année)
philologie (trimestriellement)
théologie orthodoxe (semestriellement)
théologie catholique (trois apparitions / année)
théologie greco-catholique - Varadiensis (semestriellement)
théologie catholique - Latina (annuellement)
théologie réformée - (semestriellement)
éducation physique (semestriellement)

web: http://www.studia.ubbcluj.ro   e-mail: office@studia.ubbcluj.ro